

ACCEPTED MANUSCRIPT

# Nonequilibrium electron and phonon dynamics in advanced concept solar cells

To cite this article before publication: Raghuraj Hathwar *et al* 2018 *J. Phys. D: Appl. Phys.* in press <https://doi.org/10.1088/1361-6463/aaf750>

## Manuscript version: Accepted Manuscript

Accepted Manuscript is “the version of the article accepted for publication including all changes made as a result of the peer review process, and which may also include the addition to the article by IOP Publishing of a header, an article ID, a cover sheet and/or an ‘Accepted Manuscript’ watermark, but excluding any other editing, typesetting or other changes made by IOP Publishing and/or its licensors”

This Accepted Manuscript is © 2018 IOP Publishing Ltd.

During the embargo period (the 12 month period from the publication of the Version of Record of this article), the Accepted Manuscript is fully protected by copyright and cannot be reused or reposted elsewhere.

As the Version of Record of this article is going to be / has been published on a subscription basis, this Accepted Manuscript is available for reuse under a CC BY-NC-ND 3.0 licence after the 12 month embargo period.

After the embargo period, everyone is permitted to use copy and redistribute this article for non-commercial purposes only, provided that they adhere to all the terms of the licence <https://creativecommons.org/licenses/by-nc-nd/3.0>

Although reasonable endeavours have been taken to obtain all necessary permissions from third parties to include their copyrighted content within this article, their full citation and copyright line may not be present in this Accepted Manuscript version. Before using any content from this article, please refer to the Version of Record on IOPscience once published for full citation and copyright details, as permissions will likely be required. All third party content is fully copyright protected, unless specifically stated otherwise in the figure caption in the Version of Record.

View the [article online](#) for updates and enhancements.

# Nonequilibrium Electron and Phonon Dynamics in Advanced Concept Solar Cells

R. Hathwar<sup>1,2</sup>, Y. Zou<sup>1</sup>, C. Jirauschek<sup>3</sup>, and S. M. Goodnick<sup>1</sup>

<sup>1</sup> School of Electrical Computer and Energy Engineering, Tempe AZ, USA

<sup>2</sup> Coventor Inc., a Lam Research Company, Boston MA, USA

<sup>3</sup> Department of Electrical and Computer Engineering, Technical University of Munich, Germany

E-mail: [stephen.goodnick@asu.edu](mailto:stephen.goodnick@asu.edu)

Received xxxxxx

Accepted for publication xxxxxx

Published xxxxxx

## Abstract

The realization of advanced concept solar cells that circumvent assumptions inherent in the Shockley-Queisser limit depends strongly on a competition between carrier energy relaxation processes to the lattice and high energy processes that do useful work. Here we review the role of ultrafast carrier dynamics in the performance of such advanced concept devices, experimental results to date, and then present theoretical studies of such processes using ensemble Monte Carlo simulation of electrons, holes and phonons, with a particular focus on such processes in multi-quantum well systems, as well as III-V nanowires.

Keywords: photovoltaic, nonequilibrium, ultrafast carrier dynamics, hot carriers, Monte Carlo simulation, multiexciton generation

## 1. Introduction

Far-from-equilibrium systems remain one of the least understood phenomena affecting diverse scientific fields, from molecular biology to cosmology, due to the richness and complexity of their behavior, including dissipative structures and self-organization [1]. Despite substantial research over the past 30 years on the ultrafast, nonequilibrium carrier relaxation dynamics in semiconductors, a comprehensive theoretical understanding of complex particle dynamics in low-dimensional nanostructured materials, which amplify the effects of external driving forces and suppress energy relaxation channels, is far from complete.

Early ultrafast optical excitation experiments and corresponding theoretical modeling in semiconductor bulk and quantum well systems [2] elucidated the time evolution of photoexcited electrons and holes from the femtosecond (fs) time scale through to nanoseconds and beyond. Initially, carriers evolve over several hundred fs from an athermal distribution at the excitation energy toward a heated Maxwell-Boltzmann (or Fermi-Dirac) distribution, due to strong intercarrier interactions [3] referred to as thermalization. This evolution illustrates Boltzmann's celebrated H-theorem [4],

which connects the reversible mechanics of physics with the irreversible nature of the 2<sup>nd</sup> law of thermodynamics. At even shorter times (a few fs), there are strong coherent quantum mechanical memory effects between the photoexcited charges and the optical field, which result in a rich variety of phenomena [5]. During the thermalization stage, strong electron-phonon coupling between electrons and optical phonons is the primary energy loss channel for electrons.

Finding ways to control and reduce electron-phonon energy relaxation has long been a goal of the scientific community. The quantum cascade laser [6], based on intersubband transitions in superlattices, is an elegant demonstration of the control of electron-phonon interactions in a nanostructured system to enhance radiative transitions. Its operation in a stable steady state, far-from-equilibrium, is an excellent example of a dissipative structure [1] with technological importance in energy conversion as a coherent mid-infrared and more recently terahertz (THz) radiation source [7].

If electron-phonon interactions could be mitigated or controlled, energy converters would then operate near the fundamental limits of thermodynamics, while microprocessors would operate at power levels approaching the Landauer limit [8], orders of magnitude below present

technology, enabling new, energy-efficient electronic, photonic, and computational engines.

The realization of advanced concept solar cells that circumvent assumptions inherent in the Shockley-Queisser limit (S-Q limit, [9]) depends strongly on a competition between carrier energy relaxation processes to the lattice and high energy processes that do useful work. A review of such 'third generation photovoltaics' is detailed in Ref. [10]. For example, in the hot carrier solar cell architecture [11], energetic carriers must be extracted from a nonequilibrium population of electrons and holes with average energy well above that of the background lattice temperature. Hence, the efficacy of this approach depends on a competition between the optical energy injected into the system, and ultrafast relaxation processes between electrons, holes and phonons. Another advanced concept approach is multi-exciton generation (MEG) [12,13], in which energetic electrons (holes) generated by high energy photons have sufficient excess energy to create an additional electron hole pair before relaxing in energy through competing electron-phonon interactions. Control of such interactions in bulk materials is typically difficult. However, nanostructured systems offer advantages in terms of reduced channels for energy relaxation in reduced dimensional systems, and the possibility of bandgap engineered structures for improved collection and charge separation.

The main purpose of the present topical review is to review the connection between ultrafast carrier dynamics and advanced concept solar cells, and then present numerical simulation results based using particle based simulation to elucidate these connections. It is not intended as a general review of current state of the art in photovoltaics, we refer the interested reader to recent books and web based tutorials on the subject [14,15], as well as numerous review articles on specific solar cell technologies (Si, thin film, concentrating PV, organic, etc.). Here we first give an overview of some advanced concept approaches to improving the solar to electrical energy efficiency compared to present commercial technology, the role of electron and phonon dynamics in their realization, and the current state of the art. We then discuss some of the experimental studies of electron-phonon dynamics in semiconductors with a particular emphasis on such processes in nanostructured systems such as quantum wells, nanowires and quantum dots. Finally, we discuss the use of ensemble Monte Carlo simulation of electrons, holes, and phonons to simulate ultrafast carrier relaxation processes, providing an overview of the technique, and then focusing on modeling and simulation of such dynamics in two advanced concept devices approaches, hot carrier extraction and multi-exciton generation.

In the case of hot carrier solar cell architectures, we have simulated carrier relaxation dynamics including the dynamical nonequilibrium population of optical phonons generated in III-V quantum well structures through primarily polar optical phonon emission, assuming a phenomenological anharmonic phonon decay time from an optical mode to two acoustic modes. Acoustic modes primarily propagate the excess energy away as classical heat conduction, whereas the energy of the

optical modes is retained within the optical excitation volume due to the low group velocity of such modes.

We have further simulated the role of electron-phonon scattering and impact ionization in nanowires using an atomistic tight binding representation of the nanowires, and calculating the full multi-subband impact ionization rate from perturbation theory. The percentage of electrons undergoing an impact ionizing event, thereby creating multiple electron hole pairs, is found to increase substantially above the threshold given by twice the bandgap of the nanowire, showing a strong potential for multiexciton generation in such systems, in agreement with recent experimental studies of MEG in nanowires systems.

## 2. Advanced Concept Solar Cell Structures

### 2.1 Solar Cell Operation and Efficiency Limits

Solar cell operation in semiconductors is based on the quantum mechanical process of excitation of an electron in the valence band (VB) across an energy gap to unoccupied states in the conduction band (CB) through absorption of photons with energy greater than the bandgap of the material. The most common configuration is a p-n junction diode device in which the space charge region at the junction serves to separate electrons and holes in opposite directions due to the large electric field there, giving rise to a photocurrent proportional to the photon flux incident on the device, usually synonymous with the short-circuit current ( $I_{sc}$ ) of the diode under illumination.

When this photocurrent drives a resistive load delivering power to the external circuit, a forward voltage develops across the junction which produces a 'dark' current in the opposite direction of the photocurrent. Open circuit voltage ( $V_{oc}$ ) conditions occur when the dark current exactly cancels the photocurrent, which defines the maximum voltage that power can be delivered to the external circuit. The maximum power delivered to the circuit occurs at a point less than the open circuit voltage and short circuit current, depending on microscopic origins of the dark current as well as parasitic resistances in the structure defined by the fill factor ( $FF$ ), such that the maximum power of the cell is  $P_{max} = FFV_{oc}I_{sc}$ . The optical to electrical energy conversion efficiency is then the ratio of  $P_{max}$  over the total incident power  $P_{opt}$ .

From a purely thermodynamic viewpoint, the conversion of solar energy to electrical energy, treating the source and absorber as black-body sources, should approach the Carnot efficiency, which is quite high given the effective temperature of the sun (5778 K) relative to the earth. More realistic consideration of the entropy generation in the energy conversion process results in the so-called Landsberg limit [16] of 93.3%. Further considerations of entropy generation in both the absorption and emission of radiation by a black-body source lead to a lower thermodynamic limit of 85.4% (see Ref. [10]).

In contrast, the highest reported conversion efficiency under normal intensity for a single junction solar cell is currently 28.8% for a heterojunction AlGaAs/GaAs single

crystal solar cell [17], while Si based cells have now reached over 26% [18], and perovskite based materials are rapidly approaching similar values [19]. The main reason for this large difference between current technology and the thermodynamic limits above is the broadband nature of the solar spectrum relative to a single bandgap semiconductor, which has optimum performance for only a narrow range of photon energies just above the bandgap. Photon energies below the bandgap are not absorbed, the so called transparency issue. On the other hand, for photon energies greater than the bandgap, the excess energies of the photoexcited electron and hole are rapidly lost due to electron-phonon relaxation processes, and lost to the environment in the form of heat primarily. This second loss mechanism in terms of the conversion efficiency is often referred to as thermalization loss in the photovoltaics community, although this term is used in the ultrafast community for only the short time dynamics from a completely athermal distribution to a heated Maxwell-Boltzmann or Fermi-Dirac distribution as discussed later. Clearly the transparency issue is dominant in high bandgap solar cells whereas thermalization loss dominates in small bandgap devices.

Shockley and Queisser [9] modeled the maximum conversion efficiency as a function of bandgap using a detailed balance approach representing the thermodynamic limit for a single gap absorber. Here the sun and the cell are both treated as black-body sources, where the black-body radiation from the cell corresponds to the non-equilibrium emission of a single gap system described by separate electron and hole quasi-Fermi energies, the separation of which corresponds to the external potential. The corresponding dark current is that feeding the radiative recombination driving this emission, assuming one electron-hole pair per photon (both for absorption and emission). The approach may be generalized for any input spectrum.

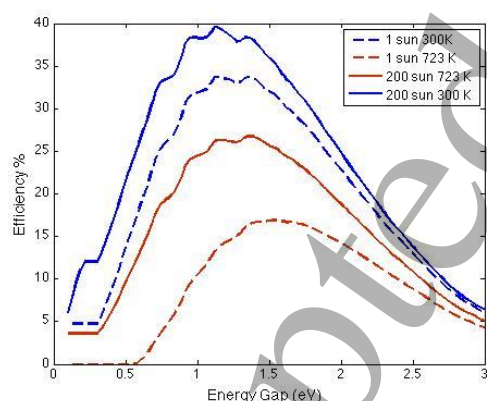


**Figure 1.** Detailed balance calculation for the AM1.5 spectrum showing the effect of temperature and concentration.

Figure 1 shows the calculated result using detailed balance for the AM1.5 solar spectrum for two different temperatures and concentrations. Consider the 300K case first; the efficiency versus bandgap peaks for a bandgap energy around 1.2 eV with a second peak at about 1.4, close to the bandgaps of Si and GaAs at 300K, with a peak value of 33.7%, the S-Q

limit. The multiple peaks reflect the spectral features at the surface of the earth due to absorption and scattering in the atmosphere, compared to an ideal black-body spectrum in outer space. The trend in overall shape is due to the trade-off between thermalization loss for low bandgaps, and transparency loss for larger bandgaps, relative to the exact nature of the solar spectrum. The increase in efficiency with concentration reflects the larger  $V_{oc}$  with increased photocurrent, which increases logarithmically with short circuit current, and thermodynamically can be associated with reduced entropy loss due to reduced acceptance angle of the cell. The degradation with temperature is expected thermodynamically in terms of increased entropy loss in the absorber, and microscopically is due to the exponential increase in the dark current with temperature.

There are various pathways to approaching thermodynamic conversion efficiencies rather than the single gap S-Q limit, by circumventing the assumptions inherent in the S-Q analysis. As mentioned above the fact that the solar spectrum is a broad band source leads to the trade-offs between transparency to below bandgap photons and thermalization energy losses for those above. If the solar spectrum could be transformed to a narrower spectrum, higher efficiency performance is possible. Up/down conversion of the solar spectrum through phosphors or two-photon absorption/emission are potential methods to accomplish this.

The S-Q analysis assumes a single electron-hole pair (ehp) excitation per photon, but the excess energy of the photon above the gap may be sufficient to produce a second or third, etc. ehp. Another route to exceeding the single gap limit is to generate multiple electron-hole pairs from a single photon through the creation of secondary carriers. The process of impact ionization in semiconductors by high energy charge carriers is well known, and the potential considered for photovoltaics [20]. More recently, nanostructured systems such as quantum dots and nanowires have shown particularly promising results due to quantum confinement effects, where the effect is often referred to as multi-exciton generation (MEG), due to the importance of excitonic states in strongly confined systems [21].

To circumvent the loss associated with thermalization (the loss of excess kinetic energy of photoexcited carriers), Ross and Nozik proposed the concept of hot carrier solar cells [11]. In this concept, electrons and holes are not collected at the band edges (which limits the output voltage to the bandgap), rather they are collected through energy selective contacts above and below the conduction and valence band edges respectively, effectively increasing the operating voltage. The absorber material suppresses energy loss, so that hot carriers can reach sufficient energy to escape through the energy selective contacts. The concept was extended further by Würfel and co-workers who considered the effect of impact ionization and secondary carrier generation on the ultimate efficiency of this concept [22,23]. Recent results are discussed in more detail later in Section 2.2.

Finally, the S-Q analysis considered only a single gap material, but already in the mid-1950s, it was recognized that multi-junction or tandem solar cells were capable of



efficiencies above that of single gap devices. Tandem solar cells have shown the highest efficiencies of any solar cell technology [24], with the record to date in excess of 46% in a four junction structure [25], which greatly exceeds the single gap S-Q limit. The detailed balance approach given by Eq. 5 can be generalized to consider multiple junctions, each with its own detailed balance equation, and with a modified spectrum according to the number of cells above or below (due to reabsorption of emitted light) the particular junction in question. Concentration provides a significant improvement in performance for high number of junctions, which can be explained simplistically in terms of Eq. (3) for the open circuit voltage increase with photocurrent (proportional to concentration) and having junctions in series where the effect is additive, multiplying the concentration effect. For maximum concentration (set by étendue limits to 46,050X), one can approach the thermodynamic limit with an arbitrarily large number of junctions.

As discussed earlier, commercial tandem cells are grown in series using epitaxial material growth technology, which is generally quite expensive compared to conventional Si solar cell manufacturing, and has many material challenges to both optimize the bandgaps and have lattice matched materials for low defect growth. There has been a recent revival in interest in Si tandem solar cells, e.g. increasing the efficiency of current Si technology with an additional junction grown on a Si substrate, to improve the performance without a substantial cost increase. For a 1.12 eV lower bandgap material, the optimum bandgap for a top material is 1.7 eV. Based on lattice matching considerations, GaP is one of the few that is nearly lattice matched to Si, and can be an alternative to a-Si as a heterojunction technology [26]. Its 2.36 eV bandgap is unsuitable for monolithic tandem applications, which has led to consideration of dilute nitride materials in order to match both bandgap and lattice constant [27].

Rather than fabricating multiple junctions, another approach is to introduce multiple levels within the same material, which provide multiple paths for photon absorption, but collect carriers at the primary bandgap of the host material. Luque and Marti introduced the concept of an intermediate band (IB) solar cell to realize such a structure, and overcome the S-Q limit [28], while similar concepts had been suggested for quantum well solar cells. An intermediate level in the bandgap is introduced through for example self-assembled quantum dots, which allow low energy photons to excite electron hole pairs through multi-photon absorption, below the gap of the principal absorber.

## 2.2 Hot Carrier Solar Cells

As discussed earlier, Ross and Nozik proposed the concept of hot carrier solar cells [11] more than 35 years ago. The main idea is to mitigate the loss due to electron-phonon processes of the excess kinetic energy of photoexcited carriers as a means to circumvent the limitations imposed by the Shockley-Queisser limit. Figure 2 shows a schematic of the basic concept. In the absorber, the loss of excess kinetic energy to the environment (i.e. the lattice) is suppressed, while

the carriers themselves still interact through carrier-carrier scattering strongly to establish a thermalized distribution, such that the electrons (and holes) are characterized by an effective temperature,  $T_H$  (or separate electron and hole temperatures as discussed in Section 4.4), much greater than the lattice temperature,  $T_L$ . This carrier temperature can be so large as to reverse the net chemical potential difference,  $\mu_{eh}$ , between electrons and holes, and typically must be on the order of a thousand degrees or more for efficient operation.

Since the average kinetic energy above the band edge is no longer lost, the tradeoff between bandgap and efficiency (Figure 1) is relaxed, and hence maximum efficiency occurs for vanishingly small absorber bandgaps leading to maximum photon absorption, although in practice a non-zero bandgap is required due to other effects.

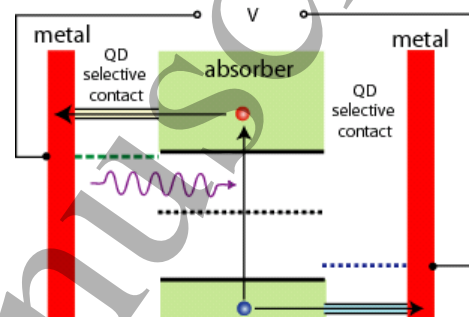


**Figure 2.** Schematic of a hot-carrier solar cell consisting of an ideal absorber with energy selective contacts [29].

Energy selective contacts are made to the absorber on the left and right, where the left contact extracts hot electrons in a narrow range of energies above the conduction band edge as shown, while the contact on the right extracts holes (injects electrons) at a specific energy range in the valence band. In this scheme, the electrons and holes are extracted from the system before they have time to relax their excess energy, hence utilizing the total energy of the photon. Under the assumption of no energy loss, the maximum efficiency occurs for vanishingly small bandgaps, hence capturing photons over the entire solar spectrum. In this limit, the theoretical detailed balance conversion efficiency approaches the maximum thermodynamic conversion efficiency of 85.4% [16]. Later, Würfel and coworkers considered the effect of impact ionization and secondary carrier generation on the ultimate efficiency of this concept [22,23].

There are many practical limitations to implementing this very ideal structure. One difficulty is realizing energy selective contacts. Würfel pointed out [22] that it is necessary to spatially separate the absorber material for the cold metallic contacts themselves, which may serve as an energy loss mechanism to the carriers in the absorber layer. It is well known, for example, that carrier drag between two spatially separated quantum wells occurs over separations on the order of nanometers [30], which means that carrier-carrier scattering between the absorber and the electrons in the contact could transfer energy from the hot absorber electrons to the contacts representing loss. A large bandgap material such as GaN could serve as a spacer or 'membrane' separating the absorber

from the contacts. Other proposals for energy selective contacts include using nanostructured resonant tunneling contacts from double barrier heterostructures, defects, or artificial quantum dots [31].

The main challenge for the hot carrier solar cell concept is to realize an ideal absorber in which the excess kinetic energy of the photoexcited carriers is not lost to the environment. Energy relaxation in bulk semiconductor materials like InAs and GaAs is dominated by longitudinal optical phonon emission via the Fröhlich interaction discussed in Section 4.4.1, which occurs on a subpicosecond time scale, which is too fast for any appreciable carrier heating even for concentrated solar light. Due to the reduced dimensionality and therefore reduced density of final states in nanostructured systems, the energy loss rate due to phonons may be reduced, which has been observed experimentally [32], and discussed in more detail in Section 3.3. In particular, in nanostructured systems such as quantum wells, quantum wires, or quantum dots, where intersubband spacing between levels is less than the optical phonon energy, then the optical emission rate may be suppressed due to the so-called ‘phonon bottleneck’ effect, since there is no final states for the electron. However, even in such systems, the reduced phonon emission rate is still too fast for sufficient carrier heating, even under high solar concentration. For quantum wires and quantum dots, reduced dimensionality effects play a larger role in energy relaxation, as we discuss in more detail later. Further, in reduced dimensional systems, phonon transport may be modified as well, which may reduce cooling as well.

If, for example, the energy is retained in the coupled electron-phonon system, then the energy may be recycled through hot phonon re-absorption. Nonequilibrium hot phonon effects during ultrafast photoexcitation have been well studied for many years, as discussed in Section 3.3. Ensemble Monte (EMC) simulation has previously been used to theoretically model ultrafast carrier relaxation and hot phonon effects in quantum well and bulk materials [33,34], where hot phonons have been shown to significantly reduce the rate of carrier cooling compared to the bare energy loss rate, as we discuss in Section 4.2.

Optical pump and probe studies discussed more in the next sections have demonstrated reduced carrier cooling in quantum wells, nanowires and nanoparticles, showing the potential of realizing absorber materials that can reach very high electron and hole temperatures. Recently, researchers have demonstrated hot carrier cell architectures that show hot carrier transfer from quantum well absorbers to contacts [35], and even photovoltaic conversion efficiencies above 10% [36].

### 2.3 Intermediate Band Devices

Intermediate band (IB) solar cells, first suggested by Luque and Marti [28,37], consist of an intermediate band between the conduction and valence band. This is shown conceptually in Figure 3 for both quantum dots and quantum wells inserted within a wider bandgap material. Impurity bands and bulk intermediate band materials have also been proposed as ways

of realizing the sort of three level structure shown. As can be seen, longer wavelength light (relative to the wider gap material) can be absorbed creating excess electrons in the intermediate state, and driving this state or band out of equilibrium. A second photon can then promote these electrons from the intermediate band to the conduction band of the high bandgap materials. Doped *n* and *p*-regions in the widebandgap materials then ideal would provide a cell voltage determined by the wide bandgap material but with increased current collection associated with the broader spectral response of the well material, circumventing the S-Q limit.

In order to realize increased efficiency, it is critical that the intermediate band population is out of equilibrium with respect to the CB or VB, i.e. that the IB has its own quasi-Fermi level. If the quasi-Fermi energies are the same for the CB and IB, then the device operates more or less at a voltage determined by the narrower gap material. Thus, the IB approach depends on achieving three sets of simultaneous absorption/radiative emission processes, each having similar magnitudes, which in turn depends on realizing multiple quasi-Fermi levels. In connection with ultrafast processes, electron-phonon scattering works against maintaining independent population through relaxation of carriers from the CB towards the lowest energy of the IB, a form of non-radiative recombination between the CB and IB. Hence, reducing the electron-phonon coupling would also be beneficial for effective operation of IB photovoltaic devices.

Assuming ideal conditions, detailed balance can be used to calculate the maximum conversion efficiency. From detailed balance, an optimum host bandgap and IB level giving maximum efficiency can be estimated. Luque and Marti showed through this analysis that an optimum combination of host bandgap (1.95 eV) and intermediate band energy (0.71 eV) leads to a maximum conversion efficiency of greater than 60 % under concentration.

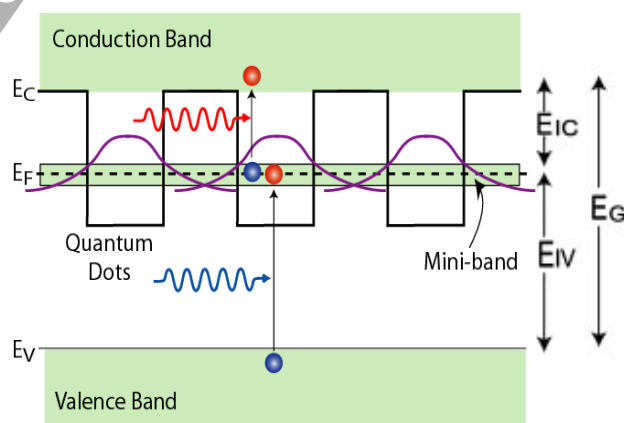


**Figure 3.** Band diagram illustrating the realization of an intermediate band solar cell using either quantum dots or quantum wells [29].

There is strong experimental evidence of the individual absorption processes shown in Figure 3 [38-42]. Marti *et al.* have demonstrated the ability to utilize two low energy photons to collect carriers at a higher energy, a necessary

prerequisite for the IB effect [43]. However, demonstration of separate nonequilibrium populations in the CB, IB and VB is ambiguous, and improved performance beyond that of the cell efficiencies of the separate materials has not been demonstrated convincingly to date, at least with respect to the best performance of the individual materials, although progress continues in this regard [44]. Of particular recent interest has been the concept of an intermediate band photon ratchet [45], in which additional states, either in close to the CB or the IB, provide secondary long lifetime states for carriers to relax to, and hence enhance the ability to maintain separately controlled carrier populations.

## 2.4 Multi-Exciton Generation Phenomena

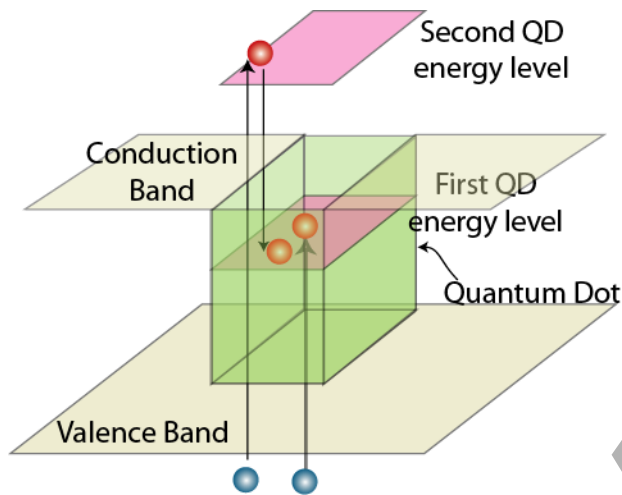


**Figure 4.** Multi-exciton generation in semiconductor quantum dots, giving rise to carrier multiplication.

Generation of multiple electron hole pairs has been known in bulk materials since the 1960's in Ge, and demonstrated experimentally in bulk silicon solar cells [20]. However, due to the constraints of both energy and crystal momentum conservation in 3D crystals, impact ionization or Auger generation processes have a low efficiency, and too high a threshold energy for effective utilization of the solar spectrum. On the other hand, nanostructured materials in which momentum conservation is relaxed have been shown experimentally to increase the efficiency of carrier multiplication processes, with lower thresholds for carrier multiplication, and experimental demonstration of multiple exciton generation (MEG) in materials such as PbSe and PbS colloidal quantum dots [46,47], with quantum efficiencies well in excess of 300%. The term multi-exciton is used in such quantum dot structures since due to the strong confinement which localizes the electron and hole in the same space, optical absorption occurs via exciton generation rather than free electron-hole pairs. Figure 4 illustrates the MEG process in which photon with energy in excess of twice the fundamental gap (including quantization and the exciton binding energy) results in two excitons (bi-exciton) generated by one photon. Recent experimental evidence [48], as well as theoretical calculations [49], suggest indeed that the multi-

excitation of several electron-hole pairs by single photons in quantum dot structures occurs at ultra-short time scales, without the necessity of impact ionization, although this is still an open question, which is hard to differentiate experimentally. Overall, MEG generation has been shown in multiple materials, including PbSe, PbS, InAs [50], PbTe [51], Si [52], CdSe [53].

In terms of the S-Q limit, the assumption that only one electron-hole pair per incident photon is generated is lifted with multi-carrier or MEG, which leads to theoretically higher efficiencies. Using detailed balance, and assuming a step-like increase in the quantum efficiency at each multiple of the bandgap, Hanna and Nozik [54] calculated a maximum efficiency of close to 44.4% under AM1.5 conditions with no concentration for a bandgap of 0.7 eV.

There have been relatively few realizations of MEG based solar cells. One difficulty is the extraction of photogenerated carriers from quantum dots in a solar cell architecture, since they are in localized states within the nanoparticle. PbSe quantum dot solar cells were reported in which for short wavelengths, quantum efficiencies (correct for reflection) greater than 100% were measured [55], which is promising.

Multiexciton generation has been measured relatively recently in PbSe nanowire/nanorod structures [56], where the threshold for enhanced quantum yield was lower than that of nanoparticles of the same material. This result is promising for MEG based solar cells since nanowire (NW) solar cells reported by Sol Voltaics and Lund University using GaAs self-assembled NWs have already reached efficiencies of 15.3% [57]. Nanowires provide a natural pathway for carrier extraction along the NW axis, and therefore efficient MEG in NW structures offers the potential to increase the efficiency in such solar cells. Numerical simulation of the carrier relaxation dynamics and multicarrier excitation in NWs are discussed in more detail in Section 4.5.

## 3. Ultrafast Electron and Phonon Dynamics in Semiconductors

### 3.1 Basic Concepts

The evolution of the electron, hole and phonon systems under ultrafast optical excitation is typically far from equilibrium, requiring a description of the dynamics that is strongly nonlinear with respect to the equilibrium state. As discussed in more detail in Section 4, the theoretical description requires a coupled set of kinetic equations, which at the most fundamental level are equations of motion for the density matrices representing the electron and phonon systems. These equations are coupled to one another through the interactions among particles as well as the interaction with the optical field of the excitation.

#### 3.1.1 Scattering processes

The most important interactions in terms of energy loss from the electron system to the environment are through electron-phonon scattering processes. Phonons are primarily classified in terms of optical or acoustic modes. Acoustic modes



correspond to lattice distortion waves in which the atomic displacements are in phase, and are characterized at long wavelengths by a linear dispersion approaching zero for small wavevectors, and with a group velocity associated with the sound velocity in the crystal. Optical phonons on the other hand are associated with the out of phase vibrations of the atoms within the basis of the unit cell, and have zero group velocity at long wavelengths and finite frequency or energy for small wavevectors. The optical phonon energies in semiconductors are on the order of 20-100 meV, and hence interact with infrared light. Both acoustic and optical modes are further classified in terms of longitudinal and transverse in terms of the atomic displacements relative to the direction of propagation, although this distinction is blurred away from the Brillouin zone center. The distinction between optical and acoustic is further complicated in nanostructured materials due to zone-folding and surface effects.

The primary electron-phonon interaction mechanism in semiconductors is described by the deformation potential Ansatz [58], in which the change in energy of the electron system with a dialation of the crystal lattice due to phonons is associated with a scattering potential, both for acoustic and optical phonons. This deformation potential is traditionally described by a single deformation potential or constant, although in general, it is an anisotropic function of wavevector, and related to the strain properties of the material. Sometimes this type of scattering is differentiated based on simplified multi-valley models of the conduction band in typical semiconductors, in terms of intravalley and intervalley phonon scattering.

Besides deformation potential scattering, polar materials which lack inversion symmetry, representative of all the III-V semiconductor materials, have an additional electrostatic component due to the difference in net charge of the basis atoms. Longitudinal polar optical phonon scattering is typically the strongest mechanism close to the conduction band edge in the III-Vs, which is described by the Fröhlich interaction [59] associated with the fluctuating dipole moment of the cation-anion pair. Similarly, for acoustic modes, the dipole moment per unit volume associated with strain leads to an additional piezoelectric component of scattering for acoustic phonons in polar materials.

### 3.1.2 Electron-phonon dynamics during ultrafast optical excitation

Ultrafast optical spectroscopic methods provide a wealth of information concerning the dynamics of electrons, holes, and phonons in semiconductors and semiconductor nanostructures on time scales ranging from a few femtoseconds through hundreds of picoseconds [5]. Typically pump and probe techniques are employed, in which an ultrafast laser pulse is used to create a nonequilibrium electron-hole plasma, and a variety of time-resolved spectroscopic techniques discussed in Section 3.2 are utilized to characterize the time evolution of this coupled electron-hole system and its subsequent interaction with the host material through electron-phonon processes.

A schematic representation of the evolution of the electron-hole system is illustrated in Figure 5. The ultrafast optical pulse produces a pulse shaped (e.g. Gaussian) distribution of electrons and holes at excess energies above the conduction and valence band edges, whose widths in energy depend on the spectral broadening of the pulse, and the pulse duration. At very short times (10s of femtoseconds), there is a strong interaction and memory effect between the optical pulse and the excitation, where coherence and memory effects dominate, and a fully quantum kinetic description is necessary. For longer times, the memory of the initial state decays, and the athermal distributions of carriers exchange energy through intercarrier interactions, both single particle and collective (screening, plasmons) on time scales of the order of several hundred fs. These interparticle interactions drive the athermal distribution towards a heated Maxwell-Boltzmann (MB) or Fermi-Dirac (FD) distribution due to the strong intercarrier interactions, referred to as thermalization. This evolution illustrates Boltzmann's celebrated H-theorem [4], which connects the reversible mechanics of physics with the irreversible nature of the 2<sup>nd</sup> law of thermodynamics. At the same time, during this thermalization process, electrons and holes begin to interact with optical phonons on time scales associated with the inverse scattering rates, over time scales of a hundred or more fs, particularly for high energy carries, where a cascade of phonon emission (and absorption) events occur. While the carrier distributions now have formed quasi-equilibrium distributions, they are out of equilibrium with lattice, and can be characterized by an electron or hole temperature,  $T_e$  or  $T_h$ , greater than the lattice temperature,  $T_L$ .

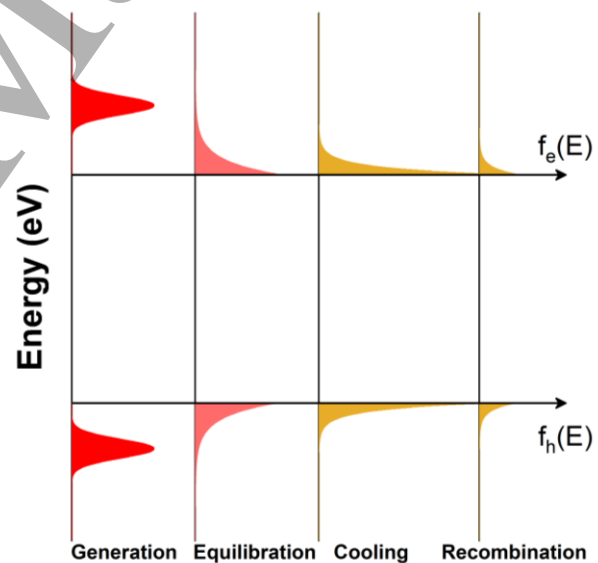


**Figure 5.** Illustration of the time evolution of the electron and hole distribution functions at various times after ultrafast optical excitation.

For longer times, thermalized electrons and holes cool through optical and acoustic phonon interactions. Acoustic modes are characterized by a group velocity on the order of the sound velocity in the solid, and so propagate energy out of the excitation volume to the environment. Optical phonons,



on the other hand, have a small group velocity, and so remain in the excitation volume, until they themselves decay into acoustic modes through anharmonic phonon-phonon interactions (3 particle or more) [60]. This phonon lifetime is measured from transient Raman scattering measurements in bulk semiconductors to be several picoseconds, much longer than the electron-phonon scattering time. Hence a nonequilibrium population of optical phonons can build-up, which in turn increases optical phonon absorption which is proportional to  $N_q$ , the phonon occupancy. The net result is a reduction in cooling [61], compared to the bare electron phonon rate.

The electron-optical phonon scattering rate is orders of magnitude higher than that of acoustic phonons, and therefore dominates the initial cooling. While acoustic phonons can have infinitesimally small energy, and thus allow the electrons to reach thermodynamic equilibrium through infinitesimal exchange of energy with the environment, optical phonons have a single threshold at  $\hbar\omega_o$ , the optical phonon energy, which for example is 36 meV for longitudinal modes in GaAs. If one considers a simple model of a constant electron-longitudinal optical phonon scattering time,  $\tau_{lo}$ , then the energy loss rate due to phonon emission alone (at low temperatures for example) is:

$$\frac{\partial E}{\partial t} = \frac{\hbar\omega_o}{\tau_{lo}} \Theta(E - \hbar\omega_o) \quad (1)$$

where  $\Theta$  is the unit step function. Averaging the energy loss over a heated MB distribution characterized by an electron temperature  $T_e$ , and assuming an ideal 2D system where the average energy of a MB distribution is  $k_b T_e$ , where  $k_b$  is Boltzmann's constant, the time rate of change of the electron temperature may be written:

$$\frac{\partial T_e}{\partial t} = \frac{\hbar\omega_o}{\tau_{lo} k_b} e^{-\frac{\hbar\omega_o}{k_b T_e}} \quad (2)$$

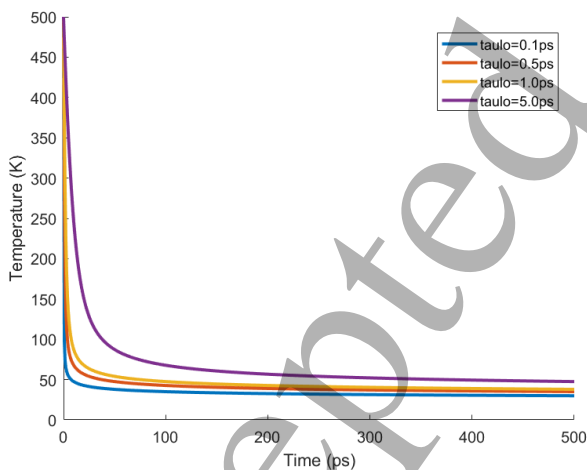


**Figure 6.** Plot of the electron temperature versus time for an initial temperature of 500 K, and various values of  $\tau_{lo}$ .

Since  $T_e$  is a function of time, this is a transcendental equation that cannot be solved analytically. A plot of the numerical solution for  $T_e(t)$  is shown in Figure 6. For this simple model of a single threshold phonon mode (the phonon energy is taken

as 35 meV), there is a rapid initial decay which reflects the phonon scattering time, and then a long time regime in which the distribution cannot cool further due to the fact that the tail of the electron distribution above the threshold is vanishingly small at this temperature. A mechanism such as acoustic phonons is therefore necessary to reach equilibrium with the lattice, which occurs on a time scale of 100s of picoseconds.

At longer times, as illustrated in Figure 5, the nonequilibrium population of cooled electrons and holes recombine through various recombination processes, reducing the carrier concentrations back to equilibrium over time scales on the order of nanoseconds and beyond.

### 3.2 Experimental Measurement Techniques

There are various techniques for characterizing ultrafast electron and phonon dynamics. The majority involve ultrafast spectroscopy [5], and in particular *pump and probe* measurements, where an ultrashort optical pulse [62], for example, is used to excite nonequilibrium electron-hole pairs (ehps), and a second probe beam of much lower intensity is used to perform time resolved spectroscopic measurements at various time delays with respect to the initial pulse.

Depending on the spectroscopic technique, different information is obtained about the time evolution of the photoexcited carriers as well as phonons, which is of particular relevance to photovoltaic devices, which are fundamentally based on photoexcitation of ehps. A wealth of information is obtained from such experiments, which probe not only the single particle states of the system in terms of the electron and hole occupancies, but coherent dynamics associated with the time evolution of the polarization of the correlated ehp, exciton dynamics, many body effects, etc.

In terms of our interest in electron, hole and phonon dynamics and their connection to advanced concepts for photovoltaics such as hot carrier solar cells and MEG, there are several spectroscopic techniques of particular interest. One important technique is transient absorption (or reflection) spectroscopy, in which the probe pulse measures the transient absorption at a single frequency,  $\nu$ , or over a range of wavelengths. For low-level excitation, the differential transmission is proportional to the sum of the electron and hole occupancies:

$$\Delta T(h\nu, t) / T_o = f_e(\mathbf{k}, t) + f_h(\mathbf{k}, t), \quad (3)$$

where  $f_e(\mathbf{k}, t)$  and  $f_h(\mathbf{k}, t)$  are the time-dependent electron and hole distribution functions for wavevector  $\mathbf{k}$  coupled by a photon of energy  $h\nu$ , where  $h$  is Planck's constant. In nanomaterials, crystal momentum is only conserved in the non-confined direction of the material, and for quantum dots, it is not conserved at all, so one probes the occupancy of states in the valence and conduction bands separated by energy  $h\nu$  for all possible states. Transient absorption spectroscopy is a powerful technique for characterizing the subpicosecond thermalization of electrons and holes, as well as the multiplication of carriers or excitons in the case of quantum dots, through MEG type processes.

Another technique that is particularly useful in characterizing electron and hole energy relaxation is time resolved photoluminescence spectroscopy (TRPL). The downward radiative recombination rate responsible for luminescence depends on the probability the initial state in the CB is occupied, and the final state in the VB is empty. Hence, the luminescence intensity may be written:

$$L(h\nu) = \alpha(h\nu) f_e(\mathbf{k}, t) f_h(\mathbf{k}, t), \quad (4)$$

where  $\alpha(h\nu)$  is the absorption coefficient corresponding to the photon energy emitted,  $h\nu$ , and  $\mathbf{k}$  is the wavevector connected by the initial and final state. By fitting the high energy tail of the luminescence spectrum with a Maxwell-Boltzmann distribution for the distribution functions above, an electron (hole) temperature as a function of time may be extracted, which gives direct information on the hot carrier energy loss rates, of particular interest in hot carrier solar cells.

Terahertz (THz) spectroscopy is another technique that provides information on excitations with characteristic in this frequency range overlapping the far-infrared regime. Excitons, phonons, and plasmons all have characteristic energies that couple in this regime. The level spacings in semiconductor nanostructures such as quantum wells, nanowires and nanoparticles also are probed by far-infrared and THz radiation. Coherent sources of THz radiation are produced by quantum cascade lasers and free electron lasers. Time domain THz pulses may be produced using photoconductive switching via ultrafast optical excitation of a semiconductor with an internal field (e.g. a space charge region) that accelerates electrons and holes in opposite directions, giving rise to a time dependent radiation in the THz range.

Ultrafast Raman spectroscopy, on the other hand, provides direct information on the phonon dynamics, particularly optical phonons, during ultrafast optical excitation [63], as well as providing information on electron-phonon coupling constants. In time-resolved inelastic light scattering (Raman scattering), the anti-Stokes line corresponding to phonon absorption, is separated from the elastic peak (Rayleigh scattering), and is proportional to  $N_q(t)$ , the phonon occupancy for phonon wavevector  $\mathbf{q}$  coupling to the light. During ultrafast photoexcitation of nonequilibrium electrons and holes, the optical phonon population is driven out of equilibrium due to emission of phonons by the charge carriers. The initial rise of the anti-Stokes Raman signal is associated with the characteristic emission times (subpicosecond) of optical phonons, whereas the decay of the anti-Stokes signal measures the decay of optical phonons by anharmonic phonon-phonon processes, hence a measure of the optical phonon lifetime.

While Raman provides indirect measurement of anharmonic phonon process, more recently ultrafast electron diffraction (UED) has emerged as a direct probe of the atomic motion [64,65]. In this technique, a train of ultra-short femtosecond pulses of high energy electrons, generated by short pulse x-rays for example in an electron gun, are incident on a material, producing a diffraction pattern. Through time

delay and reconstruction, the temporal evolution of the diffraction is measured, which in turn contains information on the time-dependent motion of the atoms. When combined with ultrafast pulse techniques to drive the lattice out of equilibrium, the time dependent anharmonic decay process at every phonon wavevector in the material may be probed.

### 3.3 Experimental Studies in Quantum Wells, Nanowires and Quantum Dots.

There have been numerous studies of ultrafast carrier dynamics in semiconductors and semiconductor nanostructures since the 1980's, which is well beyond the scope of the present paper to review. Rather, we review some of the main experimental studies relevant to advanced concept solar cells, mainly those related to hot carrier cooling, nonequilibrium phonons, and carrier multiplication (MEG) in nanostructures. Hence we are mainly interested in the thermalization and cooling phase of the carrier dynamics illustrated in Figure 5, and not on the short term, coherent phenomena on the femtosecond time scale, although such effects could be critical, for example with regard to the MEG process.

Reduced carrier cooling has been observed in low dimensional systems in many experiments [5,66]. Early experiments in quantum wells [67,68], show reduced carrier cooling during optical pumping compared to bulk systems. More recently in connection with attempts to find suitable hot carrier solar cell absorbers, researchers using both steady state and transient optical pumping in multi-quantum well systems have shown strong evidence of a nonequilibrium population of electrons and holes with average energies well above the thermal energy of the lattice [69,70,71,36]. Le Bris *et al.* [69] studied thermalization in GaInAsSb based multi-quantum well structures, where temperatures up to 200 K above the lattice temperature were measured with increasing continuous wave (CW) laser excitation coupled with PL spectroscopy. Hirst *et al.* studied both CW and transient PL in InGaAs/GaAsP multi-quantum well structures with laser excitation powers equivalent to 10,000 suns concentration, and found similar increases in carrier temperature rise with CW excitation, and higher values with TRPL, and surprising long energy relaxation times on the order of nanoseconds. Strong heating effects were also reported in type II InAs/AlAsSb MQW structures [71]. More recently, Nguyen *et al.* found carrier heating over 1400 K under strong laser excitation (50,000 suns equivalent), where they also demonstrated a working hot carrier architecture as mentioned earlier.

1D (NWs) and 0D (nanoparticles, quantum dots) are more confined, and so dimensionality effects on scattering are stronger. Long carrier relaxation times of several 100 ps were reported in InP NWs, both using transient Rayleigh scattering [72] and electron temperature rises of several 100 C in steady state photoluminescence under optical pumping [73]. In quantum dots, in which a discrete spectrum of states exist, carrier relaxation via phonon processes is further reduced due to so-called 'phonon bottleneck' effects [74,75,76], where the

relaxation dynamics can be mediated by polaronic [77] and Auger effects [78].

As discussed in Section 4, while long energy relaxation times are measured in low dimensional systems, such long energy relaxation times cannot be explained in most cases by the electron-phonon scattering rate, which are not that different from the bulk rates in QWs and NWs. Rather, other processes must play a role, in particular the role of the nonequilibrium evolution of the corresponding lattice excitations (phonons) responsible for carrier thermalization, which have long been known to play a critical role in reducing the cooling rate of photoexcited hot carriers [61,79]. Nonequilibrium hot phonon effects during ultrafast photoexcitation have been studied for many years. As discussed in the previous section, time-resolved Raman scattering has been used to characterize the optical phonon decay after photoexcitation for a variety of III-V compound bulk and quantum well materials [80,81,82,83]. The main observations from such studies is that the anharmonic decay time for phonons is in the range of 1 to 10 ps for both types of systems. As discussed in Section 4.4, such phonon decay times are still too short for appreciably high carrier temperatures for example in QW systems.

Recent work has focused on decreasing the decay rate of optical phonons to acoustic modes (which couple to the environment) through *phononic* materials where the lowest order decay modes are suppressed [84,85]. The main requirement is to have a *phononic bandgap* between the highest lying acoustic phonon branches and the lowest optical modes, such that decay via the so called Klemens mechanism [60] is suppressed due to energy and crystal momentum conservation. Among the common semiconductors, InN has such a phonon dispersion, and recent results from the UNSW on InGaN materials have demonstrated greatly reduced energy relaxation rates from TRPL measurements, suggestive of the role of nonequilibrium phonons [71]. However, the theoretical understanding of the coupled electron-phonon dynamics responsible for slow cooling in nanostructured materials remains unresolved, and new techniques to simulate and characterize both the nonequilibrium electron and phonon dynamics simultaneously across the full Brillouin zone are needed.

Two-dimensional materials such as graphene, and the dichalcogenides [86], offer new opportunities to develop a basic understanding of far-from-equilibrium behavior in nanoscale systems and to conceptualize material architectures that control and exploit electron-phonon interactions in diverse settings. Unique carrier relaxation dynamics have been shown in quasi-2D materials [87], while hybrid perovskite materials have recently demonstrated slow energy relaxation rates [88] and nonequilibrium phonon effects [89].

## 4. Theoretical Modelling of Electron-Phonon Dynamics

### 4.1 Overview

The theoretical description of electron-phonon dynamics is treated at various levels of sophistication from fully quantum mechanical descriptions to semi-classical based on solution of the Boltzmann transport equation (BTE). In particular, as mentioned earlier, in comparing to studies of ultrafast carrier dynamics in which carriers are generated by femtosecond laser pulses, quantum coherence effects are quite strong at short times, and further, the change in carrier (or phonon) populations due to either the external excitation or scattering events cannot be included on the same footing in the BTE [90]. For longer times (100s of fs), most coherent effects relative to memory of the initial state have decayed, and the dynamics is dominated by incoherent interactions between quasi-particles.

At the most fundamental level, the full dynamics of electrons and phonons are governed by the quantum Liouville equation for the density matrix, which in principle contains all the information possible about the system including the external environment. In practice, this many body problem is too difficult to solve, and approximations are necessary to reduce the problem to one that can be solved numerically. One approach is using the full time-dependent solutions of the Kadanoff-Baym equations (KBEs) [91], which are quantum kinetic equations based on nonequilibrium Green's functions (NEGF) [92,93]. Another approach from the standpoint of ultrafast dynamics has been use of reduced density matrix approaches to deriving quantum kinetic equations for single particle quantities such as distribution functions and polarization [94]. In particular, a popular form of this reduced density matrix approach are the 'semiconductor Bloch equations', representing coupled equations for the polarization and carrier distributions [95].

For longer times (100s of fs), coherent memory effects of the initial excitation have mostly decayed, and the interactions between electrons, holes, and phonons may be treated within the Markovian approximation, i.e. that scattering destroys the memory of the state before scattering, corresponding to incoherent dynamics. In the semi-classical description of transport, we further assume that the occupancy of electron (hole) and phonon states may be described by single particle distribution functions  $f(\mathbf{r}, \mathbf{k}, t)$  and  $g(\mathbf{r}, \mathbf{q}, t)$ , respectively, that simultaneously specify the probability of occupancy of a state at position  $\mathbf{r}$  and crystal momentum  $\mathbf{k}$  for electrons and  $\mathbf{q}$  for the phonons. Then the coupled semi-classical BTE for electrons (holes) and phonons may be written:

$$\left( \frac{\partial}{\partial t} + v_e(\mathbf{k}) \cdot \nabla_{\mathbf{r}} + \frac{e}{\hbar} E(\mathbf{r}) \cdot \nabla_{\mathbf{k}} \right) f = \sum_{\mathbf{q}} \left\{ W_{e,q}^{k+q \rightarrow k} + W_{a,-q}^{k+q \rightarrow k} - W_{e,-q}^{k \rightarrow k+q} - W_{a,q}^{k \rightarrow k+q} \right\} \quad (5)$$

$$\left( \frac{\partial}{\partial t} + v_p(\mathbf{q}) \cdot \nabla_{\mathbf{r}} \right) g = \sum_{\mathbf{k}} \left\{ W_{e,q}^{k+q \rightarrow k} - W_{a,q}^{k \rightarrow k+q} \right\} + \left( \frac{\partial g}{\partial t} \right)_{p-p}$$

Here,  $W_{e,q}^{k+q \rightarrow k}$  is the probability for electron transition from  $k+q$  to  $k$  due to emission of phonon  $q$ . Similarly  $W_{a,q}^{k+q \rightarrow k}$  refers to processes of absorption.  $v_e$  and  $v_p$  represent the

electron and phonon group velocities respectively. The last term on the right-hand side accounts for anharmonic phonon-phonon scattering processes. The system is nonlinear, as the probabilities  $W$  depend on the product  $fg$  of the electron and phonon distribution functions, as well as higher powers of  $f$  and  $g$  in terms of electron-electron and phonon-phonon scattering.

The solution of the BTE itself is a six-dimensional problem in the phase space of position and momentum, which is challenging to solve directly. There are various approximations used to solve the electron and phonon BTEs, such as the relaxation time approximation for scattering, which is only valid close to equilibrium, and moment expansions of the BTE, assuming some model form for the electron and phonon distribution functions. In dealing with far from equilibrium systems involving strong driving forces such as high electric fields or strong optical pumping, the most widespread approach is the statistical solution of the BTE using Monte Carlo methods, which is discussed next.

#### 4.2 Ensemble Monte Carlo Simulation of Electrons and Holes

The Ensemble Monte Carlo (EMC) technique has been used since the 1970s as a stochastic method to simulate nonequilibrium transport in semiconductor materials and devices [96,97,98]. The basic technique is to simulate the free particle motion (referred to as the free flight) terminated by instantaneous random scattering events. The Monte Carlo algorithm consists of generating random free flight times for each particle, choosing the type of scattering occurring at the end of the free flight, changing the final energy and momentum of the particle after scattering, and then repeating the procedure for the next free flight. By simulating an *ensemble* of particles representative of the physical system of interest which are synchronized at each time-step, the non-stationary time-dependent evolution of the charge carrier and phonon distributions under the influence of time-dependent external driving forces may be simulated. In application to ultrafast optical experiments, the particle distribution functions have a direct connection to the time evolution of optical absorption, luminescence and the anti-Stokes Raman intensity for example as discussed earlier.

The EMC method described above (and in more detail below) is different in implementation from that of *kinetic Monte Carlo* (KMC) simulation, which is based on the same random scattering approach to transport. However, KMC simulation is generally event based, meaning a series of random events are simulated for a particle with no time step, and the steady state behavior is statistically constructed from simulation of numerous different trajectories. This has the advantage of simulating fast and slow processes that may occur over orders of magnitude different time scales, as occurs in hopping conduction through disordered materials. It has been used for example in the simulation of organic solar cells [99] and thermoelectrics [100]. The EMC approach is more appropriate for time dependent transient simulation such as

that relevant to ultrafast carrier dynamics, the topic of the present paper.

As mentioned earlier, in the Monte Carlo method, the dynamics of a particle in momentum space is decomposed into random free flights terminated by instantaneous, memoryless, scattering events, similar to the assumptions inherent in the BTE. Writing the probability for scattering in the time interval  $dt$  around time  $t$  as  $W(\mathbf{k}(t))dt$ , where  $W(\mathbf{k}(t))$  is the total scattering rate of a particle of wavevector  $\mathbf{k}(t)$ , the probability of scattering in the time interval  $dt$  after a free flight of time  $t$  may be written as the joint probability:

$$P(t)dt = W[\mathbf{k}(t)] \exp\left[-\int_0^t W[\mathbf{k}(t')]dt'\right] dt. \quad (6)$$

Random flight times may be generated according to the probability density  $P(t)$  above using pseudo-random numbers generated numerically which are uniformly distributed random numbers in the range  $[0,1]$ . Random flight times sampled from  $P(t)$  may be generated according to:

$$r = \int_0^{t_r} P(t)dt, \quad (7)$$

where  $r$  is a uniformly distributed random number, and  $t_r$  is the desired free flight time. Integrating Eq. (7) with  $P(t)$  given by Eq. (6) above yields:

$$r = 1 - \exp\left[-\int_0^{t_r} W[\mathbf{k}(t')]dt'\right]. \quad (8)$$

Since  $1-r$  is statistically the same as  $r$ , Eq. (8) may be simplified to read:

$$-\ln r = \int_0^{t_r} W[\mathbf{k}(t')]dt'. \quad (9)$$

Numerically, rather than integrating the time dependent  $W$  along the trajectory of the particle which is time-consuming, a fictitious *self-scattering* mechanism is introduced which changes neither the energy or momentum of the particle such that the total scattering rate of all real scattering processes plus this self-scattering is a constant:

$$W = W[\mathbf{k}(t')] + W_{\text{self}}[\mathbf{k}(t')], \quad (10)$$

where  $W_{\text{self}}[\mathbf{k}(t')]$  is the self-scattering rate. Hence, Eq. (9) above becomes simply:

$$t_r = -\frac{1}{W} \ln r. \quad (11)$$

In this way, the random free flight time is chosen after every scattering event for every particle in the ensemble. The constant total rate (including self-scattering)  $\Gamma$  is chosen *a priori* so that it is larger than the maximum scattering encountered during the simulation interval.

The total scattering rate for electrons,  $W$ , is the sum of the real scattering rates due to phonon absorption and emission, ionized impurities, surface roughness, intercarrier scattering, etc. plus self-scattering (assuming collision events are uncorrelated):

$$W = W_{\text{self}}[n, \mathbf{k}] + W_1[n, \mathbf{k}] + W_2[n, \mathbf{k}] + \dots W_N[n, \mathbf{k}] \quad (12)$$



with  $n$  the band index of the particle (or subband in the case of reduced-dimensionality systems), and  $\mathbf{k}$  the wavevector at the end of the free-flight. The scattering rates are typically pre-tabulated in a look-up table at the beginning of the simulation. The type of scattering at the end of the free flight is then selected randomly according to the relative weights in the sum above to the total scattering.

The final wavevector after scattering is chosen randomly according to the scattering cross-section for each mechanism, and energy conservation. In the case of self-scattering, neither the energy or wavevector are changed, hence it has no effect on the dynamics, rather it is a convenient tool for simplifying the scattering/free flight algorithm, and allows complicated scattering processes to be included that change dynamically during the simulation, such as multi-carrier scattering processes.

Early EMC simulations of carrier transport were based on simplified representations of the electronic band structure in terms of multiple parabolic or nonparabolic bands, sometimes referred to as multi-valley EMC. *Full band Monte Carlo* [98,101] refers to numerically including the full electronic band structure from density functional theory (DFT), or semi-empirical methods such as the empirical pseudopotential method or the tight binding approximation. The carrier free flights in  $\mathbf{k}$ -space remain the same, however the final state after scattering involves a search through the first Brillouin zone for the final state, which can be numerically demanding. The full band cellular Monte Carlo method [102] stores the total rate for every  $\mathbf{k}$  to every possible  $\mathbf{k}'$  in the first Brillouin zone, so that the final state is chosen by a single random number, leading to significant speedup, at the cost of increased memory.

### 4.3 Simulation of Phonon Dynamics

Solution of the phonon BTE, Eq. (5), by Monte Carlo methods has been reported by a number of authors [103,104,105,106,107]. In general, one needs to solve a set of coupled phonon BTEs, one for each acoustic and optical mode, which are coupled together by phonon-phonon scattering, in addition to other scattering process such as impurity, surface scattering, isotope scattering, and electron-phonon scattering which couples the phonon BTEs to the electron BTEs.

Phonon-phonon scattering is an important multi-phonon process that is responsible for the decay of nonequilibrium optical phonons into acoustic modes, critical for the energy relaxation of an optically excited electron-phonon system such as a photovoltaic device. The phonon states and their dispersion are derived in terms of their coupled equations of motion and second quantization within the harmonic potential approximation. This harmonic potential between atoms represents the unperturbed state of the phonon system, and therefore high order anharmonic forces are treated as a perturbation resulting in phonon-phonon scattering [108]. The rate at which a phonon with wavevector  $\mathbf{q}$  decays into two phonons with final wavevectors  $\mathbf{q}'$  and  $\mathbf{q}''$  may be written:

$$W_d(\mathbf{q}, \mathbf{q}', \mathbf{q}'') = n_{\mathbf{q}}(n_{\mathbf{q}'} + 1)(n_{\mathbf{q}''} + 1)A(\mathbf{q}, \mathbf{q}', \mathbf{q}'') \quad (13)$$

where  $n_{\mathbf{q}}$ ,  $n_{\mathbf{q}'}$  and  $n_{\mathbf{q}''}$  are the phonon populations of the respective wavevectors of the three phonons involved (which in general correspond to different modes), and  $A$  is a population-independent term that represents the strength of the three-phonon process [60], the so-called Klemens interaction. A similar expression relates the annihilation of two phonons to create a third phonon. Higher order four phonon, etc. processes exist as well, and can provide additional decay channels. Since the various  $n$  in Eq. (13) above change dynamically in time, the direct solution is difficult. Using the self-scattering method discussed in Section 4.2, simulation of such three phonon processes including the full time dependent distributions in Eq. (13) above have been reported [109], which give good agreement with thermal conductivity data in semiconductors.

While there have been very few attempts at coupling the full electron and phonon BTEs in simulating carrier dynamics during photoexcitation, a simplified form has been employed for the dynamics of optical phonons [61,79]. In this scheme, the phonon population,  $n_{\mathbf{q}}(t)$ , is defined on a grid in momentum space, and is updated at uniform time steps during the EMC simulation. A single, phenomenological wavevector independent phonon lifetime is assumed for all phonon decay processes, although this assumption is not necessary for the algorithm. The functional dependence of  $n_{\mathbf{q}}(t)$  is obtained through the expression:

$$n_{\mathbf{q}}(t + \Delta t) = \bar{n}_{\mathbf{q}}(t) - \frac{\Delta t}{\tau_{ph}} [\bar{n}_{\mathbf{q}}(t) - N_0], \quad (14)$$

$$\bar{n}_{\mathbf{q}}(t) = n_{\mathbf{q}}(t) + \delta n_{\mathbf{q}}$$

where  $\delta n_{\mathbf{q}}$  is the net change in the phonon population during the last time step due to phonon emission and absorption through electron-phonon scattering, and  $\tau_{ph}$  is the optical phonon lifetime. The changes  $\delta n_{\mathbf{q}}$  are monitored by keeping track of all emission and absorption processes within the EMC procedure for each phonon momentum state, which itself is stored on a discretized grid in momentum space. For optical phonons, the above procedure is a fairly good approximation as the group velocity of optical phonons is quite small, and therefore the velocity term in Eq. (5) disappears. Such an approach on the other hand would not be justified for acoustic phonons.

### 4.4 Coupled Electron-Phonon Dynamics in Quantum Wells

In this section, we use the EMC model discussed in the previous two sections to model ultrafast carrier relaxation in multi-quantum well (MQW) systems including nonequilibrium phonons, using a multi-valley model for a single GaAs/AlGaAs quantum well, and discuss the connection with recent experimental investigations of slow carrier cooling in MQW systems in connection with hot carrier solar cells.

#### 4.4.1 Scattering rates

There are a variety of processes responsible for electron (hole) scattering including phonon emission and absorption, intercarrier scattering (electron-electron, electron-hole, hole-hole), impurity, alloy, and interface roughness at the boundary of the well and the barrier. Within the framework of perturbation theory, the lowest order approximation for the scattering rate of carriers by these various mechanisms is based on first order, time dependent perturbation theory. In the model, the transition rate from an initial state  $\mathbf{k}$  in band  $n$  to a final state  $\mathbf{k}'$  in band  $m$  for the  $j$ th scattering mechanism is given by Fermi's Golden rule [110]:

$$W_j[n, \mathbf{k}; m, \mathbf{k}'] = \frac{2\pi}{\hbar} \left| \langle m, \mathbf{k}' | V_j(\mathbf{r}) | n, \mathbf{k} \rangle \right|^2 \delta(E_{m\mathbf{k}'} - E_{n\mathbf{k}} \mp \hbar\omega) \quad (15)$$

where  $V_j(\mathbf{r})$  is the scattering potential of this process,  $E_{n\mathbf{k}}$  and  $E_{m\mathbf{k}'}$  are the initial and final state energies of the particle. The delta function results in conservation of energy for long times after the collision is over, with  $\hbar\omega$  the energy absorbed (upper sign) or emitted (lower sign) during the process. Equation (15) neglects effects such as collision broadening and finite collision duration, which can be substantial effects for high scattering rates and short times [111].

In quantum well materials, the motion perpendicular to the interface is quantized into a set of *subbands*, while motion parallel to the interface is characterized by propagating solutions. Therefore, in the Fermi's rule above Eq. (15), the indices  $m$  and  $n$  refer to subband index in addition to band index. For III-V materials such as GaAs, the dominant energy relaxation mechanism for electrons in the central valley below the  $\Gamma$  -  $L$  threshold is that of longitudinal polar-optical phonon (POP) emission. The POP scattering rate is described by the Fröhlich interaction described earlier. For bulk-like polar optical phonons, the scattering rate for an electron initially in subband  $n$  to a final subband  $m$  may be written [3,112]:

$$W_{nm}^{pop}(k) = \frac{eE_o}{2\hbar} \left[ \left( n_{\omega_o} + \frac{1}{2} \mp \frac{1}{2} \right) \int_0^\infty d\theta \frac{H_{nm}(q\pm)}{q\pm} \right], \quad (16)$$

Where  $e$  is the charge of an electron,  $n_{\omega_o}$  is the longitudinal optical phonon occupancy,  $q_\pm$  is the scattered wavevector in the plane parallel to the interface, and the upper and lower signs correspond to phonon absorption and emission, respectively. The effective field,  $eE_o$ , is given by:

$$eE_o = \frac{m^* e^2 \hbar \omega_o}{4\pi \hbar^2} \left( \frac{1}{\epsilon_\infty} - \frac{1}{\epsilon_0} \right), \quad (17)$$

where  $\epsilon_0$  and  $\epsilon_\infty$  are the low- and high-frequency permittivities of the material, and  $\omega_o$  is the longitudinal optical phonon frequency. The function  $H_{nm}(q_\pm)$  is given by:

$$H_{nm}(q_\pm) = \int_{-\infty}^\infty dz \rho_{nm}(z) \int_{-\infty}^\infty dz' \rho_{nm}^*(z') e^{-q_\pm |z-z'|}, \quad (18)$$

where  $\rho_{nm}(z) = \phi_n(z) \phi_m^*(z)$  is the product of the initial and final subband envelope functions, and the scattered wavevector is fixed by energy conservation to be:

$$q_\pm = |\mathbf{k} - \mathbf{k}'| = \left[ 2k^2 \pm \frac{2\omega_{nm}^* m^*}{\hbar} - 2k \left( k^2 \pm \frac{2\omega_{nm}^* m^*}{\hbar} \right)^{1/2} \cos \theta \right]^{1/2} \quad (19)$$

$$\hbar\omega_{nm}^* = \hbar\omega_o \pm (E_n - E_m),$$

where  $\hbar\omega_{nm}^*$  represents an effective phonon energy, which may be zero or negative,  $m^*$  is the effective mass, and  $E_n$  and  $E_m$  are the subband energy minima of  $n$  and  $m$  subbands respectively.

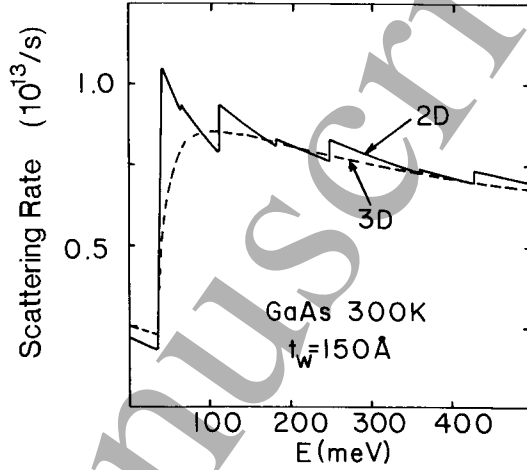


**Figure 7.** POP scattering rate versus energy for bulk GaAs and for a 15 nm GaAs/AlGaAs quantum well [3].

The total POP scattering rates versus energy for both absorption and emission are plotted in Figure 7 for bulk GaAs and for the quasi-2D rates calculated using Eq. (16) for the first subband. What is interesting to note is that the 2D rate is just a piece-wise continuous approximation of the 3D rate, where the discontinuities in the 2D rate represent the onset of intersubband scattering with higher subbands. As can be seen, the scattering rate and corresponding energy relaxation are similar to the 3D rate, and therefore greatly reduced carrier cooling is not expected in quantum well structures based on reduced dimensionality effects in the scattering rates themselves. The consideration of phonon confinement effects due to the narrow layer thicknesses, in which surface phonons and waveguide modes in the well occur, does not change this general observation significantly [113].

What can be observed is that the intersubband rate is reduced compared to the intrasubband rate, hence reduced cooling can occur due to the transfer from higher subbands to lower subbands. This effect becomes particularly noticeable in quasi-1D nanowire (NW) systems, where bottleneck effects are observed as discussed in Section 4.5.

As mentioned earlier, intercarrier scattering in terms of electron-electron and electron-hole scattering are responsible for two main effects. One is the thermalization of the athermal initial carrier distribution after ultrafast laser pumping, leading to a heated Fermi-Dirac distribution. The second is a redistribution of energy from the electron system to the hole system, which drives both distributions towards a common energy.

Inclusion of intercarrier effects represents a nonlinearity in the BTE, since such effects depend on the carrier distribution function itself. One effect is that due to degeneracy, or the effect of the final state occupancy, which for Fermions requires that the final state be empty. To include this, the bare scattering rate is modified by a factor  $1 - f_m(\mathbf{k}')$ , where  $\mathbf{k}'$  is the state after scattering. During EMC simulation,  $f_m(E')$  is typically tabulated for simplicity, and a self-scattering rejection technique used to select whether a real or self-scattering occurs using a random number between 0 and 1 in comparison to  $f_m(E')$ .

In terms of intercarrier scattering, binary collisions are modelled as a screened Coulomb potential as seen by the incident particle in a relative frame of reference to both particles' motion. In the case of bulk electrons in a single parabolic conduction band, the scattering rate for a particle of wavevector  $\mathbf{k}_0$  due to all the other particles in the ensemble is given by [114]:

$$W_{ee}(\mathbf{k}_0) = \frac{nm_n e^4}{4\pi\hbar^3 \varepsilon^2 \beta^2} \int d\mathbf{k} f(\mathbf{k}) \frac{|\mathbf{k} - \mathbf{k}_0|}{(|\mathbf{k} - \mathbf{k}_0|^2 + \beta^2)}, \quad (20)$$

where  $f(\mathbf{k})$  is the normalized one-particle distribution function,  $\varepsilon$  the permittivity,  $n$  the electron density,  $m_n$  the conduction band effective mass, and  $\beta$  is the screening constant. Similar forms occur for electron-hole scattering with  $m_n$  replaced with the reduced mass between the two particles.  $f$  is an implicit function of time, so that this rate changes dynamically with time. To treat this interaction within an EMC framework, a self-scattering rejection technique is again used [115], in which the maximum scattering rate occurs for  $f(\mathbf{k})=1$ , which allows the integral above to be solved at the beginning of the simulation, and the rate adjusted thereafter in terms of actual scattering events and value of  $f(\mathbf{k})$ . Similar forms have been derived for electrons and holes in 2D [3,116] and 1D [117] where carrier-carrier scattering leads to inter-subband as well as intra-subband electron-electron transitions.

#### 4.4.1 Simulation of Carrier Relaxation

The simulated effects of both intercarrier scattering and POP scattering on the initial dynamics of electrons during photoexcitation are shown in Figure 8 for a 10 nm QW system, including quasi-2D POP and intercarrier scattering, and including degeneracy of the final state. A simulated narrow temporal width (10 fs) pulse creates an athermal carrier distribution centered around the peak in energy of the pulse ( $\sim 150$  meV above the lowest subband energy). At short times after the pulse, optical phonon emission occurs resulting in a satellite peak separated 36 meV (the assumed LO phonon energy in GaAs) from the main peak. This develops into a series of peaks (phonon replicas) by 100 fs. After 500 fs, the peaks are already washed out due to electron-electron and electron-hole scattering, and the distribution has evolved to a heated Fermi-Dirac distribution. This distribution continues to cool with time in subsequent snapshots.

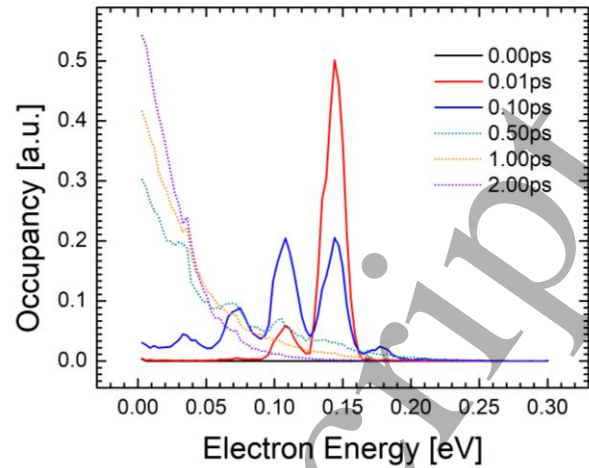


**Figure 8.** Snapshots of the electron distribution at various times following and initial pulse at time zero for a 10 nm GaAs QW at 10 K. The photon energy was chosen such that the peak of energy of the pulse is 150 meV above the lowest subband energy. The injected 2D carrier density is  $5 \times 10^{11}/\text{cm}^2$ .

One question that is of concern in the modelling of hot carrier solar cells is whether the electron and hole systems are at the same temperature relative to one another. Here degeneracy was turned off, such that the average energy of the 2D system can be equated directly to  $k_b T_{e,h}$ , and two different densities are simulated. A relatively high energy for the photoexcited carriers was simulated for two different densities, and including nonequilibrium phonons with a lifetime of 7 ps (the measured value in bulk GaAs). As can be seen in Figure 9, the temperatures of the electrons and holes approach one another, although for the higher injected density where nonequilibrium phonon effects are stronger, the two temperatures remain different for several 10s of picoseconds. This occurs partly because of the stronger scattering of holes not only with POP scattering, but deformation potential scattering as well which was included here.

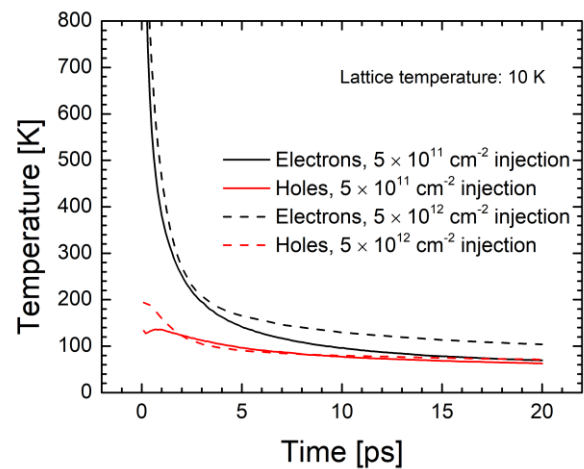


**Figure 9.** Electron and hole temperatures versus time after ultrafast excitation.

The effects of nonequilibrium phonons is included here using the model described in Eq. (14). To investigate the role of nonequilibrium phonons in the cool rates, Figure 10 shows the cooling rate for several different longitudinal optical phonon lifetimes, and two different injected carrier densities. Phonon lifetimes of 0 ps (no hot phonon effect), 7 ps (GaAs bulk lifetime), and an artificially high optical phonon lifetime of 500 ps are considered. The effect on the cooling rate is clear; in the absence of nonequilibrium optical phonons, the cooling is dominated by the bare electron-phonon scattering rate, which has a subpicosecond time-scale, and the electrons cool towards the lattice temperature in a nonlinear fashion similar to the analytical model discussed in Section 3.1.2. With the inclusion of nonequilibrium phonons, the energy relaxation is decreased, the carriers cool more slowly after an initial fast relaxation. The effect is stronger for higher injected density as the phonon population is driven more strongly out of equilibrium by the higher electron population and subsequent phonon emission.

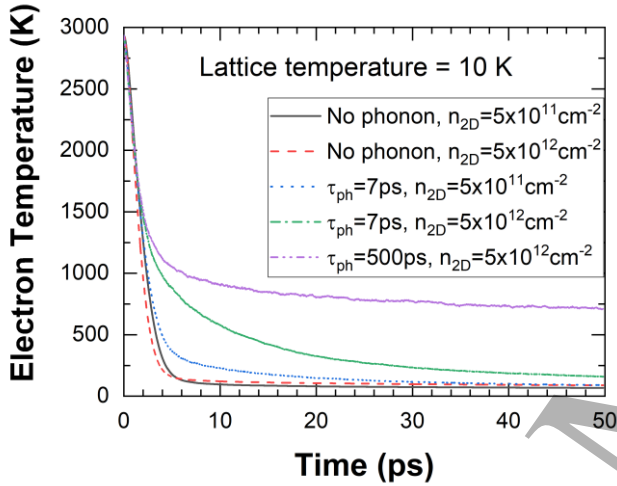


**Figure 10.** Electron temperature versus time for 0, 7, and 500 ps phonon lifetimes, and two different injected densities, considering only the conduction band.

For very long anharmonic phonon decay times, the cooling is slowed completely, and asymptotically is limited by the phonon decay and not the electron-phonon scattering rate. While not a physically realizable situation, particularly in consideration of higher order anharmonic processes, it illustrates the reduction in cooling from one dominated by POP emission to one in which the phonon lifetime dominates the cooling rate.

Figure 11 shows the POP absorption and emission rates versus time tabulated during the EMC simulation including nonequilibrium phonons. The lattice temperature is 10 K in these simulations, so that the equilibrium POP absorption rate proportional to the Bose-Einstein distribution at this temperature, is very close to zero. With the inclusion of nonequilibrium phonons, the rates of phonon emission and absorption quickly reach the same value and then decay together according to the anharmonic decay time, thus controlling the cooling rate.

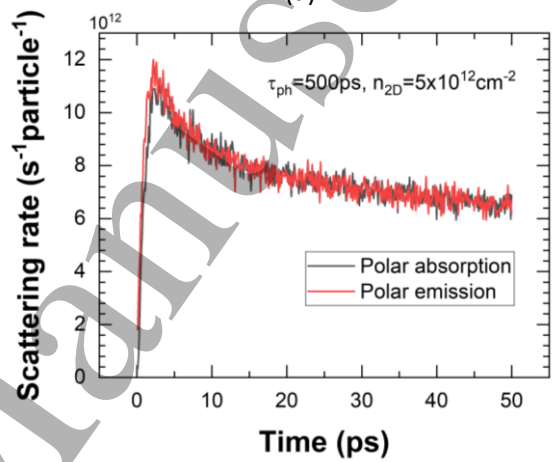
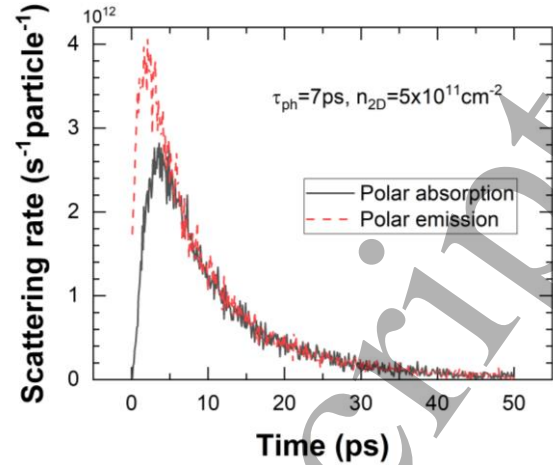


**Figure 11.** Phonon absorption and emission rates versus time after ultrafast excitation for (a)  $\tau_{ph}=7$  ps and an injected density of  $5 \times 10^{11}/\text{cm}^2$  and (b)  $\tau_{ph}=500$  ps and an injected density of  $5 \times 10^{12}/\text{cm}^2$ .

#### 4.4.3 Summary of Quantum Well Results

To summarize the results of this section, ensemble Monte Carlo simulations of ultrafast optical excitation were performed for a model GaAs/AlGaAs system to investigate the reasons and mechanisms for strong carrier heating and long carrier cooling times measured in some QW systems experimentally as discussed in Section 3.3 and earlier in connection with hot carrier solar cells. The main connection between the Monte Carlo simulations reported here and experimental studies are in terms of transient photoluminescence studies, where the carrier temperature as a function of time, where similar shape cooling curves are obtained depending on what physics is included.

The first observation is that the reduction in the scattering rates due to reduced dimensionality in QW systems play only a minor role if any. The dominant energy relaxation mechanism, LO phonon emission, is basically a piecewise continuous approximation of the bulk POP rate, with



additional channels associated with intersubband scattering, due to the continuum of states available parallel to the interface. Therefore, to first order, the decay time to the lattice temperature by 2D POP scattering alone is only a few picoseconds. The situation is not different if confinement of the phonons are considered based on previous work. This picture does not account for many body effects such as polaron formation or frequency dependent screening and electron-plasmon interactions. However, none of these effects can account for orders of magnitude differences in the bare LO phonon emission time in 2D, and rather tend to increase energy relaxation. An exception is when subbands are spatially indirect, for example when barrier states are accessed by high energy electrons as they relax, or in type II heterostructure systems, and the overlap of the envelope function between higher and lower subbands is very small [118], so that high energy carriers are 'stuck' in higher subbands over times which can approach nanoseconds. Such effects would not, however, explain satisfactorily the high carrier temperatures extracted experimentally from the high energy tail of the PL spectra, as within each subband, the carriers thermalize to the bottom of their respective subbands due to intrasubband LO emission.

Simulation of nonequilibrium phonons generated by the strong LO emission during the initial stages of relaxation, and their subsequent feedback through absorption and emission were shown to modify the energy relaxation rates of electrons from that limited by the bare LO phonon emission rate to one limited by the anharmonic decay time of LO phonons to acoustic phonons (here a phenomenological phonon lifetime was used, and the energy transferred to acoustic phonons assumed to be removed instantaneously). Such hot phonon effects can provide a explanation to the longer cooling times measured experimentally in some cases, although to explain decay times of hundreds of picoseconds, it requires assuming anharmonic decay times of the same time scale, which is contrary to the measured anharmonic decay times in normal III-V materials such as the arsenides, phosphides and antimonides, based on time resolved Raman measurements, which are less than 10 ps. This then may point to the role of nonequilibrium acoustic as well as optical modes, and how heat is transported out of confined structures on sub-nanosecond time scales, which would require full simulation of the phonon BTE for all modes, in momentum and real space.

#### 4.5 Carrier Relaxation and Multi-Exciton Generation in Nanowires

##### 4.5.1 Nanowire Electronic Structure and Scattering Rates

The full band Monte Carlo method described in Section 4.2 can also be applied to simulating nonequilibrium electron and phonon phenomena in nanowires (NWs). Here we focus only on the electron and hole systems, and not on the phonon systems, in order to understand the ultrafast relaxation dynamics due to phonon scattering in NWs, and in particular

to impact ionization processes in NWs that could be responsible for MEG effects.

First, the band structure of NWs needs to be calculated. A popular method to calculate the band structure of NWs is the empirical tight binding method (TB) [119]. To apply the method, the atomic structure of the NW needs to be constructed, as shown in Figure 12 for a 4 nm  $\text{In}_{0.53}\text{Ga}_{0.47}\text{As}$  NW with 2 nm of InP cladding, which is hexagonal in shape due to faceting during self-assembled growth. The band structure of the nanowire is calculated by setting up the Hamiltonian of the system and solving the eigenvalue problem to obtain the eigen-energies at different k-vector points along the one-dimensional Brillouin zone (BZ).

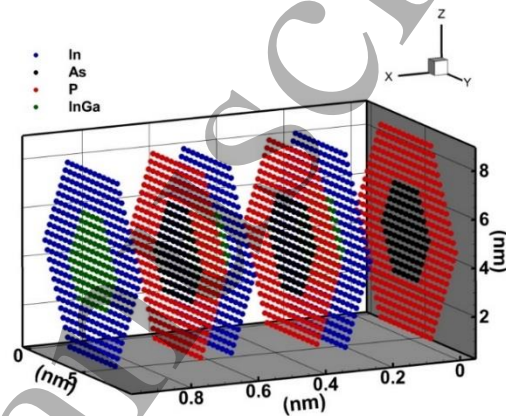


**Figure 12.** Unit cell structure of a 4 nm hexagonal  $\text{In}_{0.53}\text{Ga}_{0.47}\text{As}$  NW with 2 nm InP cladding.

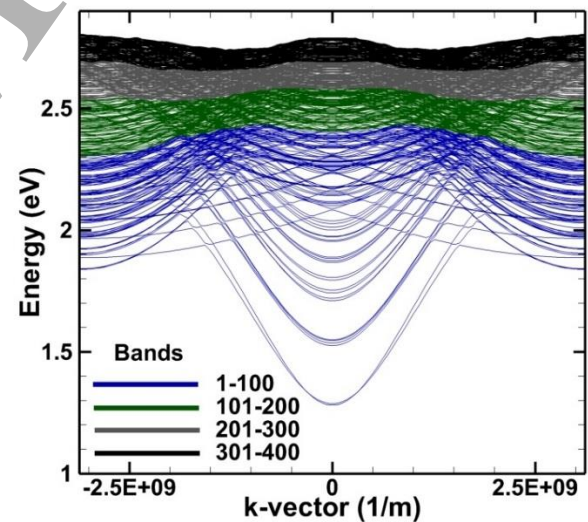


**Figure 13.** Band structure of 4 nm hexagonal  $\text{In}_{0.53}\text{Ga}_{0.47}\text{As}$  nanowire with 2 nm of InP cladding with different bands highlighted.

Figure 13 shows the first 400 bands of the one-dimensional band structure of a 4 nm  $\times$  4 nm  $\text{In}_{0.53}\text{Ga}_{0.47}\text{As}$  nanowire with 2 nm of InP cladding. As shown there, the first two degenerate subbands (including spin) are well separated in energy, while successive bands increasingly merge into a continuum of

states, whose density of states approaches that of the bulk material.

The scattering rates for nanowires are again calculated using Fermi's golden rule as:

$$W_{\mu,\nu}(k,k') = \frac{2\pi}{\hbar} |V_{k,k'}|^2 \delta(E_{\nu,k'} - E_{\mu,k} \pm \hbar\omega) \quad (21)$$

where  $k$  and  $k'$  are the initial and final wave vectors along the nanowire axis direction at band indices  $\mu$  and  $\nu$  respectively.  $V_{k,k'}$  is the matrix element for the particular scattering mechanism,  $E_{\nu,k'}$  and  $E_{\mu,k}$  are the initial and final energy states and  $\omega$  is the phonon wavenumber if it is present in the scattering mechanism. The lack of an exact description of the orbitals in the TB formulation makes the calculation of the matrix element difficult, but due to the highly local nature of the atomic orbitals, approximations can be made to calculate the overlap integrals in the matrix elements accurately [120]. To model carrier relaxation processes, the important scattering mechanisms to consider are the processes that assist energy dissipation, namely deformation potential scattering, polar optical phonon scattering and impact ionization scattering processes. The matrix element for the deformation potential scattering process is calculated using the deformation potential approximation [121]. To simplify the calculation of the matrix elements, the phonon dispersion is assumed to be bulk-like with acoustic phonons assuming a linear dispersion with the equipartition approximation and the optical phonons to be dispersionless across the BZ. With the above approximations, the deformation potential scattering rates due to acoustic and optical phonons is given by [120]:

$$W_{ac,\mu,\nu}(k_x,k'_x) = \frac{E_{ac}^2 kT}{4\pi\rho v_s^2 \hbar} I_{\mu,\nu}(q) \frac{\partial k'_x}{\partial E_{\nu}(k'_x)} \quad (22)$$

$$W_{op,\mu,\nu}(k_x,k'_x) = \frac{E_{op}^2}{4\pi\rho\omega_{op}} \left( N_{q,op} + \frac{1}{2} \pm \frac{1}{2} \right) I_{\mu,\nu}(q) \frac{\partial k'_x}{\partial E_{\nu}(k'_x)} \quad (23)$$

where

$$I_{\mu,\nu}(q) = \sum_m P_{\mu,\nu,m}^*(k_x,k'_x) \sum_{m'} P_{\mu,\nu,m'}(k_x,k'_x) \left[ e^{iq[\tau_{m,x} - \tau_{m',x}]} \int_0^{q_c} J_0(q, a_{diff}) q_i dq_i \right] \quad (24)$$

where  $J_0$  is the zeroth order Bessel function,  $a_{diff} = \sqrt{(\tau_{m,y} - \tau_{m',y})^2 + (\tau_{m,z} - \tau_{m',z})^2}$  with  $\tau_{m,y}$  representing the atomic position within the supercell of the nanowire, and the sum is over all orbitals in the supercell. The quantity  $P_{\mu,\nu,m'}$  is the product of the expansion coefficients for subbands  $\mu$  and  $\nu$  of the Wannier function of the  $m$ th atomic orbitals.  $q$  and  $q_i$  are the phonon wavevector and its parallel component in the cross-section of the nanowire, respectively, and  $q_c$  is the cut-off wave vector along the transverse direction to account for the projection of the BZ of the bulk phonons onto the confinement plane.  $E_{ac}$  and  $E_{op}$  are the deformation potential constants for the acoustic and optical modes respectively,  $v_s$  is the average sound velocity in the material [122] and  $\omega_{op}$  is the wavenumber for the optical phonons.

The polar optical phonon scattering rate in a nanowire is given by:

$$W_{pop,\mu,\nu}(k_x,k'_x) = \frac{\omega_0 e^2}{8\pi} \left[ \frac{1}{\epsilon_{\infty}} - \frac{1}{\epsilon_0} \right] \left( N_{q,op} + \frac{1}{2} \pm \frac{1}{2} \right) I_{pop,\mu,\nu}(q) \frac{\partial k'_x}{\partial E_{\nu}(k'_x)} \quad (25)$$

where

$$I_{pop,\mu,\nu}(q) = \sum_m P_{\mu,\nu,m}^*(k_x,k'_x) \sum_{m'} P_{\mu,\nu,m'}(k_x,k'_x) \left[ e^{iq[\tau_{m,x} - \tau_{m',x}]} \int_0^{q_c} \frac{J_0(q, a_{diff})}{q^2 + q_i^2} q_i dq_i \right] \quad (26)$$

where  $q_i$  is the phonon vector normal to the confinement direction. The latter integral in Eq. (26) is pre-calculated for different values of  $q$  and  $a_{diff}$  at the beginning of the simulation. This greatly improves the computational time. Figure 14 shows the comparison of the deformation and polar optical phonon scattering rates between a 2 nm  $\times$  2 nm InAs NW and bulk InAs. The same set of deformation potentials is used for both systems. At high energies the rates tend to each other as the electrons will not experience the confining potential of the NW at large energies and behave in a bulk-like fashion.

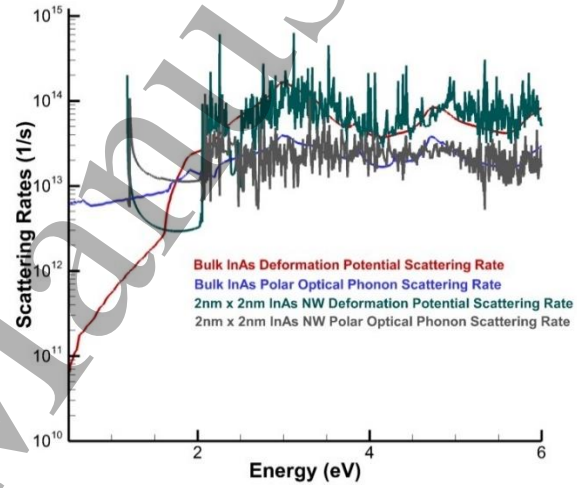


**Figure 14.** Comparison between 2 nm  $\times$  2 nm InAs nanowire and InAs bulk deformation potential and polar optical phonon scattering rates [123].

The impact ionization process is one of the main forms of energy dissipation in carriers which have very large energies. The process for electrons can be described as a high energy electron in the conduction band interacts with a hole in the valence band to produce a new electron and hole in the conduction and valence band respectively. The process for holes is similar. The matrix element for impact ionization must capture this interaction between the 4 particles and is given by [124]:

$$|M(k_{1,n}, k_{2,n'}, k_{3,m'}, k_{4,m})|^2 = \frac{1}{2} (|M_a|^2 + |M_b|^2 + |M_a - M_b|^2) \quad (27)$$

where

$$M_a = \int \langle \psi_{1,n}(k_1, r_1) \psi_{4,m}(k_4, r_2) | \frac{e^2}{4\pi\epsilon|r_1 - r_2|} | \psi_{2,n'}(k_2, r_1) \psi_{3,m'}(k_3, r_2) \rangle dr_1 dr_2$$

$$M_b = \int \langle \psi_{1,n}(k_1, r_1) \psi_{4,m}(k_4, r_2) | \frac{e^2}{4\pi\epsilon|r_1 - r_2|} | \psi_{3,m'}(k_2, r_1) \psi_{2,n'}(k_3, r_2) \rangle dr_1 dr_2 \quad (28)$$

where the electron in band  $n$ , interacts with a hole in band  $m$  to produce a new electron and hole in bands  $n'$  and  $m'$

respectively. The net impact ionization scattering rate between 2 states can be given as [120]:

$$W_{II}(k_{1,n}, \Delta k_{2,n'}) = \frac{e^4}{\hbar \epsilon^2 (2\pi)^3} \int_{E_{\min}}^{E_{\max}} \sum_{i,m,m'} \left| F_{n,n'}(k_1, k_2, k_i, k_i - (k_1 - k_2)) \right|^2 \times [JDOS_{m,m'}(k_i - (k_1 - k_2), k_i)] DOS_{n'}(k_2) dE_{n'}(k_2)$$

(29)

where JDOS represents the joint density of states. The requirement of the conservation of energy and momentum in this process constrains the number of possible interactions between the 4 particles, but the number is still very large in NWs [120]. Various approximations must be used to reduce the computational time such as the assumption of isotropy in the matrix element. Figure 15 shows a plot of the impact ionization rate as a function of energy in a 2 nm × 2 nm Si NW.

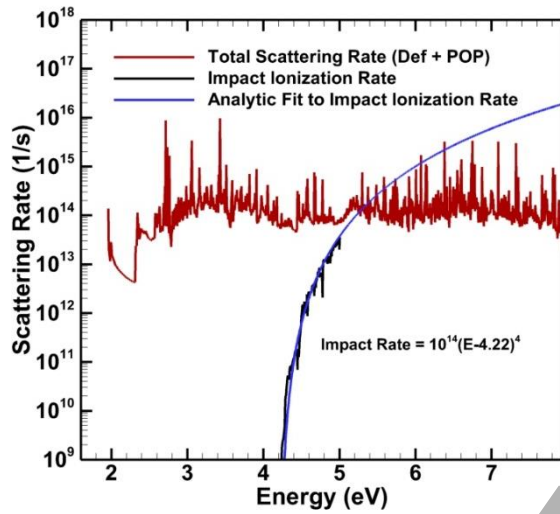


**Figure 15.** Comparison between the impact ionization scattering rate of a 2 nm × 2 nm Si nanowire and an analytical fit based on the popular power law approximation [125].

#### 4.5.2 Simulation of Carrier Dynamics in Nanowires

The analysis of energy relaxation rates is performed using a uniform field Monte Carlo simulation. To simulate hot carrier relaxation during photoexcitation, the electrons are initialized with a mean energy corresponding to the excitation energy shown in Figure 16 and a Gaussian half-width of 100 meV. After a few picoseconds, the initial distribution thermalizes and the decay is exponential as shown in Figure 17. As can be seen in Figure 16, after 5 ps, the carriers are still primarily in the upper subband, and hence there is a form of phonon bottleneck to relax to ground subband. Electron-electron scattering has not been considered here, so such processes could speed up the transfer rate between subbands.

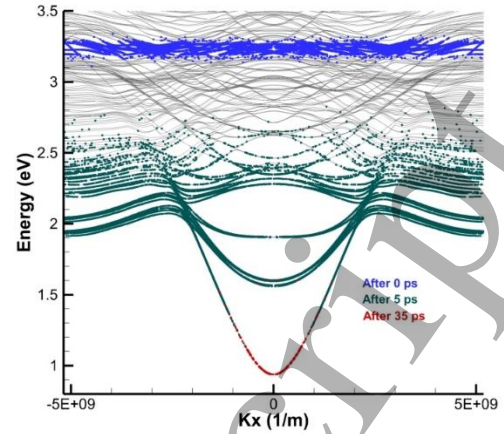


**Figure 16.** Carrier chart for a 3 nm × 3 nm InAs NW with excited electrons at  $2E_g$  for different times [123].

As shown in Figure 17, the relaxation rate in the cladded NWs is significantly slower compared to the bulk material due to the reduced overlap between carriers stuck in the cladded layer and the core NW, as well as the bottleneck effect discussed earlier. This leads to less energy dissipating scattering processes, which in turn increases the energy relaxation time of the carriers.

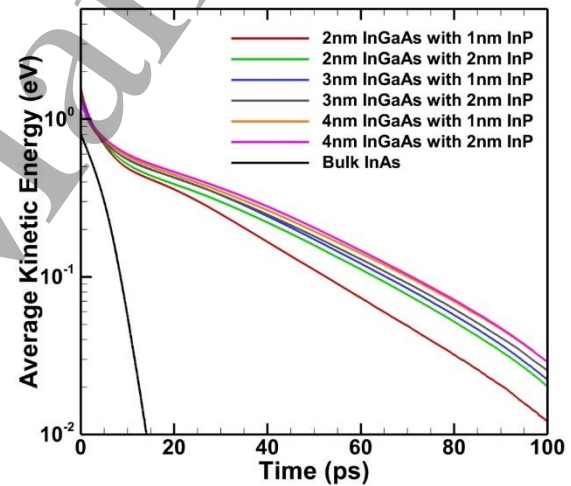


**Figure 17.** Energy relaxation of hot electrons in Bulk InAs compared with  $\text{In}_{0.53}\text{Ga}_{0.47}\text{As}$  NW with InP cladding, where the average kinetic energy is relative to the minimum of the ground subband.

The distribution of charge in the cladded NW as the energy relaxation process is underway can also be calculated from the wavefunction of the electrons. Within the TB basis, the charge around an atom is calculated. This is then summed over all electrons to obtain the spatial charge distribution. Figure 18 shows a scatter plot of the charge distribution at the beginning and end of the photoexcitation process.



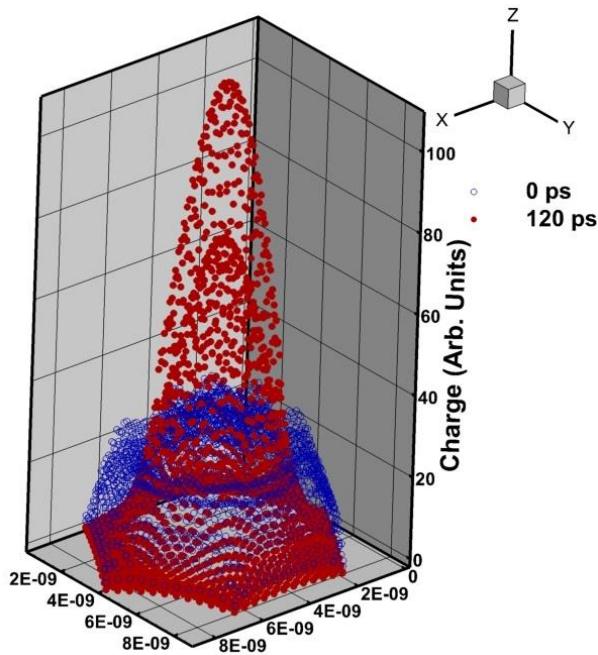


**Figure 18.** Charge distribution in a 4 nm x 4 nm  $\text{In}_{0.53}\text{Ga}_{0.47}\text{As}$  NW with 2 nm InP cladding at the instance of photoexcitation and after 120 ps of energy relaxation.

At 0 ps the charge is almost uniformly distributed across the cladded NW but as the carriers are allowed to relax, most of the charge is located in the core NW as compared to the cladded NW.

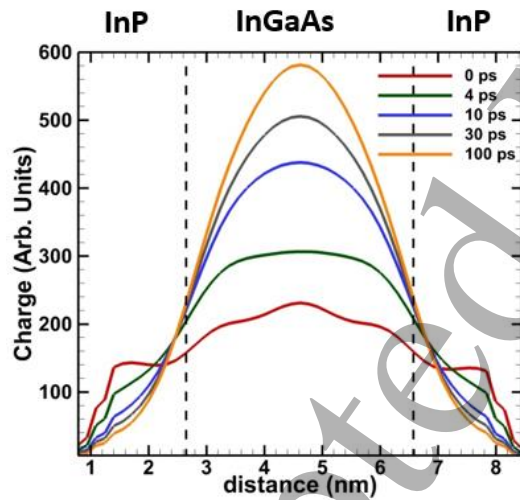


**Figure 19.** 2D distribution of charge in a 4 nm x 4 nm  $\text{In}_{0.53}\text{Ga}_{0.47}\text{As}$  NW with 2 nm InP cladding for different times after photoexcitation.

This process can be seen more clearly in the 2D charge distribution plot shown in Figure 19. As time goes on, the charge settles more in the core NW compared to the cladded NW. This is expected as the bandgap of the core NW is lesser than that of the cladded material.

The percentage of generation of electron hole pairs due to the impact ionization process can also be calculated using the Monte Carlo approach. The electron hole generation depends on the probability that an electron will undergo an impact ionization process before deformation potential scattering and polar optical phonon scattering process relax the electron's energy to below the threshold of impact ionization. The percentage of electrons undergoing an impact ionization event therefore strongly depends on the nature of the individual scattering rates. Figure 20 shows a plot of the calculated electron-hole generation as a percentage of initial electrons for different incident photon energies written in terms of multiples of the bandgap of the NW system, assuming all the kinetic energy of the incident photon is transferred to the electron. As can be seen, there is a sharp threshold for photon energies a little greater than twice the bandgap, similar to the ideal situation envisioned in MEG solar cells. A similar threshold occurs at three times the bandgap, giving a step-like quantum yield with photon energy, which resembles the ideal model of MEG.

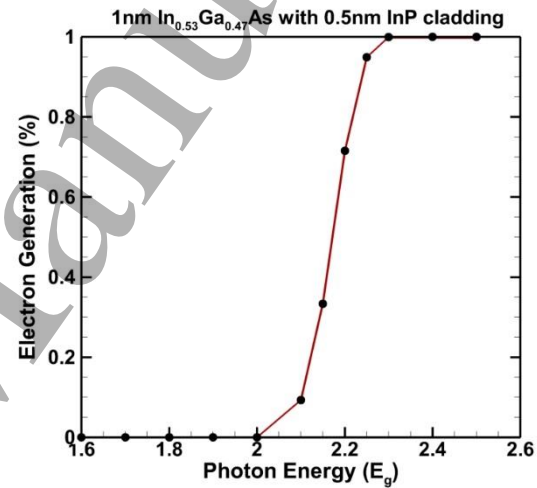


**Figure 20.** Variation of the multi-electron generation percentage with incident photon energy [123].

In reality, when electron-hole pairs are created through band to band absorption, the kinetic energy is partitioned between both the electron and hole. The common assumption often made is that the excess energy of the photon goes primarily to the electron based on the typically much higher hole masses compared to electrons at the band edge. However, when we talk about photons with energy on the order of  $2E_g$  or larger, such arguments break down as the density of states sample by photons are not that different. To study this, we looked at the optical transition rate in NWs due to direct, allowed transitions within the usual dipole approximation for the full multi-subband system calculated within the tight binding framework, where the upward transition rate may be written

$$W_{abs} = \frac{2\pi}{\hbar} \frac{e^2}{m_0^2} \left( \frac{\hbar n_{ph}}{2\omega\epsilon} \right) \sum_{states} |(a.p)_{cv}|^2 \delta(E_e - E_h - \hbar\omega)$$



where  $n_{ph}$  is the photon flux,  $(a.p)_{cv}$  is the dipole matrix element between different subbands, and  $\omega$  the photon frequency. This rate was then used to generate electrons and holes corresponding to a monochromatic incident flux of electrons during the full band Monte Carlo simulation. Figure 21 shows the initial distributions of generated electrons and holes based on the NW bandstructure. It is clear that the excess energy of the electron is significantly reduced due to the partitioning between the VB and CB in the NW, where the density of states at these energies is really more bulk-like.

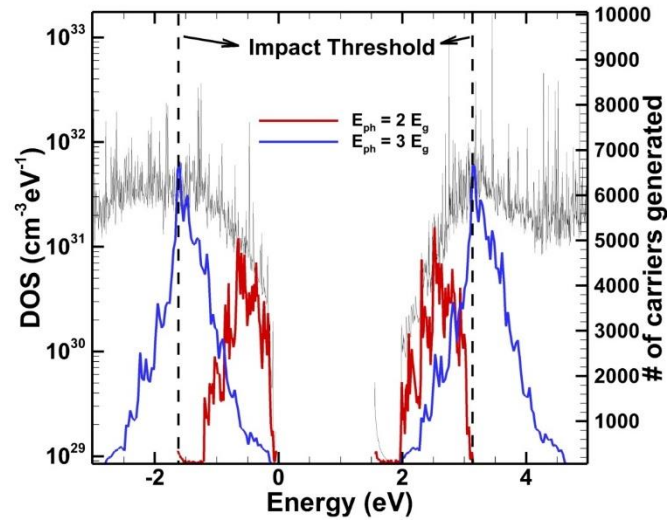


**Figure 21.** Simulated initial distributions of electrons and holes for two different photon energies,  $2E_g$  and  $3E_g$  for a 2 nm InGaAs NW with a 1 nm InP cladding.

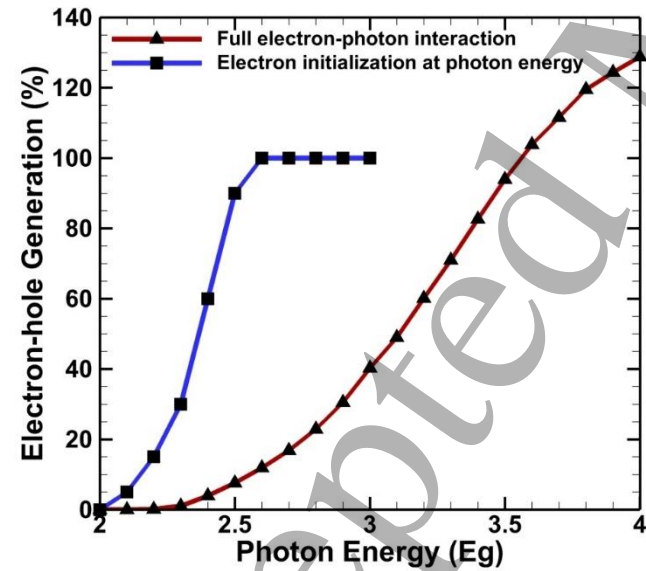


**Figure 22.** Variation of the multi-electron generation percentage with incident energy comparing the effects of kinetic energy partitioning between electrons and holes for incident photons.

The consequence for this in terms of the multi-carrier excitation (excitonic effects are not considered here), are shown in Figure 22. The MEG rate is now smeared out and a

more linear rather than step-like quantum yield is found in comparison with the assumption that all the photon energy goes into the electron. While this result indicates that in practice, the MEG rate is less pronounced in the NW systems modeled than ideally, the more linear quantum yield curve and lack of distinct plateaus is actually much closer to experimental measurement of the MEG rate in NPs and NWs.

#### 4.5.3 Summary of Nanowire Relaxation Studies

To summarize this section, we investigated energy relaxation and MEG in narrow III-V NWs using an atomistic full band approach based on the empirical tight binding method. Full-band EMC simulation was performed of the k-space dynamics of photoexcited carriers considering only various phonon relaxation process as well as impact excitation. In contrast to the QW case, we found a strong reduction in the energy relaxation rate due to the reduced dimensionality of system in terms of the 1D density of states and scattering rates, as well as real space transfer effects associated with clad NWs, which suggests that NW systems may be even more suitable for hot carrier type devices, in agreement with experimental studies on NWs showing strong heating effects.

Multi-carrier generation was investigated in connection with MEG solar cell applications, by simulating both the impact excitation process as an incoherent scattering process, and in more realistic simulation of the electron-hole generation process for high energy photons. The effect of the latter is to smear out the threshold and give rise to a more linear quantum yield curve than the ideal model for MEG devices, which may help explain the characteristic shape of the measured quantum yield curves via for example ultrafast absorption spectroscopy.

## 5. Conclusions

In this review, we have discussed the limitations of efficiency of current photovoltaic technology, and advanced concepts to realize efficiencies approaching thermodynamic maximum efficiencies rather than the single gap Shockley-Queisser limit. The dynamics of ultrafast optical excitation of electrons and holes was discussed, as well as a discussion of the theoretical modeling of such phenomena. The semi-classical ensemble Monte Carlo method was introduced, and application of this approach for ultrafast excitation in semiconductor quantum wells was presented, where the low cooling rates measured experimentally in QW systems are ascribed to nonequilibrium phonon effects. Hot carrier relaxation in ultrasmall nanowire systems was also presented, where long relaxation rates are observed in the absence of any hot phonon effects, due to phonon emission bottlenecks in relaxing to the ground subband. Multi-carrier generation was simulated as well using a full band representation of the optical generation process, which shows that NWs should be effective in applications to MEG solar cells.

The simulation results presented here support some of the current approaches to improving the performance of advanced concept solar cells as well as suggesting other avenues of

investigation. MEG in nanowires appears promising, where EMC simulation shows that the effect based on single particle impact ionization should be sufficient for good performance. The advantages nanowires over quantum dots is the natural extraction pathway for photogenerated carriers along the wire axis, which is already the basis for current nanowire solar cells.

In the case of hot carrier solar cells, clearly the optical phonon lifetime plays a critical role in maintaining the nonequilibrium hot carrier distribution necessary for high performance devices. Hence, efforts to engineer phononic bandgap materials with long anharmonic decays will help facilitate this goal. The role of acoustic phonons is, however, not well understood, and confinement of the acoustic modes such that they do not propagate heat away to the environment may lead to improved performance. Reduced dimensional systems such as nanowires or even quantum dots also leads to reduced cooling due to phonon bottleneck effects, which could improve the performance of the technology. Maintaining a nonequilibrium carrier distribution may also not require engineering electron-phonon interactions, rather trapping

carriers in upper level states, for example in the barrier states of multiquantum well structures, may allow their capture at high energies.

## Acknowledgements

This material is based upon work primarily supported by the Engineering Research Center Program of the National Science Foundation and the Office of Energy Efficiency and Renewable Energy of the Department of Energy under NSF Cooperative Agreement No. EEC- 1041895. Any opinions, findings and conclusions or recommendations expressed in this material are those of the author(s) and do not necessarily reflect those of the National Science Foundation or Department of Energy. Support was also provided through the Institute for Advanced Science (IAS) at the Technical University of Munich. C.J. acknowledges support by the German Research Foundation (DFG) within the Heisenberg program (JI 115/4-2).

## References

- [1] Prigogine I 1980 *From Being To Becoming* Freeman
- [2] Shah J 1992 *Hot Carriers in Semiconductor Microstructures: Physics and Applications* Academic Press Inc.
- [3] Goodnick S M and Lugli P 1988 *Phys. Rev. B* **37** 2578-2588
- [4] McQuarrie D A 1976 *Statistical Mechanics* Harper and Row pp 411-418
- [5] Shah J 1999 *Ultrafast Spectroscopy of Semiconductors and Semiconductor Nanostructures 2<sup>nd</sup> Ed.* Springer Series in Solid-State Sciences **115**
- [6] Faist J, Capasso F, Sivco D L, Sirtori C, Hutchinson A and Cho A Y 1994 *Science* **264** 553-556
- [7] Williams B S 2007 *Nat. Photonics* **1** 517
- [8] Landauer R 1961 *IBM Journal of Research and Development* **5** 3 183-191
- [9] Shockley W and Queisser H J 1961 *Journal of Applied Physics* **32** 510-519
- [10] Green M A 2003 *Third Generation Photovoltaics: Advanced Solar Energy Conversion* Springer-Verlag
- [11] Ross R T and Nozik A J 1982 *J. Appl. Phys.* **53**, 3813-3818
- [12] Schaller R D and Klimov V I 2004 *Physical Review Letters* **92** 186601
- [13] Ellingson R J, Beard M C, Johnson J C, Yu P, Micic O I, Nozik A J, Shabaev A and Efros A L 2005 *Nano Lett* **5** 865-871
- [14] Würfel P and Würfel U 2009 *Physics of Solar Cells: From Basic Principles to Advanced Concepts* Wiley.
- [15] PVEDucation.org
- [16] Landsberg P T and Tonge G 1980 *J. Appl. Phys.* **51**, R1-R20
- [17] Green M A, Emery K, Hishikawa Y, Warta W, Dunlap E D, Levi D H and Ho-Baillie A W Y 2017 *Prog. Photovolt: Res. Appl.* **25** 3-13
- [18] Yoshikawa K, Kawasaki H, Yoshida W, Irie T, Konishi, K., Nakano K, Uto T, Adachi D, Kanematsu M, Uzu H and Yamamoto K 2017 *Nature Energy* **2** 1
- [19] Yang W S, Noh J H, Jeon N J et al. 2015 *Science* **348** 1234
- [20] Kolodinski S, Werner J H, Wittchen T and Queisser H J 1993 *Appl. Phys. Lett.* **63** 2405
- [21] Schaller R and Klimov V 2004 *Phys. Rev. Lett.* **92** 186601
- [22] Würfel P 1997 *Sol. Energy Mater. Sol. Cells* **46** 43
- [23] Würfel P, Brown A S, Humphrey T E and Green M A 2005 *Prog. Photovolt: Res. Appl.* **13** 277
- [24] Cotal H, Fetzer C, Boisvert J, Kinsey G, King R, Hebert P, Yoon H and Karam N 2009 *Energy & Environmental Science* **2** 174-192
- [25] Press Release, Fraunhofer Institute for Solar Energy Systems, 1 December 2014 (accessed at <http://www.ise.fraunhofer.de/en/press-and-media/press-releases/press-releases-2014/new-world-record-for-solar-cell-efficiency-at-46-percent-on-7-december-2014>). Soitec record
- [26] Zhang C, Kim Y, Faleev N N and Honsberg C B 2017 *Journal of Crystal Growth* **475** 83-87
- [27] Weyers M, Sato M and Ando H 1992 *Jpn. J. Appl. Phys.* **31** L853-L955
- [28] Luque A and Martí A 1997 *Phys. Rev. Lett.* **78** 5014-5017
- [29] Goodnick S.M., Faleev N., Honsberg C. (2013) Nanoscale Photovoltaics and the Terawatt Challenge. In: *Nanoscale Applications for Information and Energy Systems. Nanostructure Science and Technology* Korkin A., Lockwood D. (eds) Springer, New York, NY
- [30] Gramila, T. J., Eisenstein, J. P., MacDonald, A. H., Pfeiffer, L. N., and West, K. W. 1991 *Phys. Rev. Lett.* **66**, 1216-1219.
- [31] Conibeer G, Green M A, Corkish R, Cho Y, Choe E, Jiang C, Fangsuwannarak T, Pink E, Huang Y, Puzzer T, Trupke T, Richards B, Shalav A and Lind K 2006 *Thin Solid Films* **654** 511-512
- [32] Pelouch W S, Ellingson R J, Powers P E, Tang C L, Szymid D M and Nozik A J 1992 *Phys. Rev. B* **45** 1450-1453
- [33] Goodnick S M and Lugli P 1992 *Hot Carriers in Semiconductor Microstructures: Physics and Applications*, (J. Shah, Ed.) Academic Press Inc. 191-234
- [34] Dür M, Goodnick S M and Lugli P 1996 *Phys. Rev. B* **54** 17794
- [35] Dimmock J A R, Day S, Kauer M, Smith K, and Heffernan J 2014 *Prog. Photovolt. Res. Appl.* **22** 151

- [36] Nguyen D T, Lombez L, Gibelli F, Boyer-Richard S, Le Corre A, Durand O and Guillemoles J F 2018 *Nature Energy* **3** 236–242
- [37] Luque A and Martí A 2010 *Adv. Mater* **22** 160–174
- [38] Yao Y, Charles W O, Tsai T, Wysocki G, Chen J and Gmachl C F 2010 *Applied Physics Letters* **96** 211106
- [39] Bhattacharya P, Stiff-Roberts A D, Krishna S and Kennerly S 2002 *International Journal of High Speed Electronics and Systems* **12** 969–94
- [40] MacMillan H F, Hamaker H C, Kaminar N R, Kuryla M S, Ristow M L, Liu D D, Virshup G F and Gee J M 1988 *IEEE Photovoltaic Specialists Conference* 462
- [41] Bailey C G, Forbes D V, Raffaele R P and Hubbard S M 2011 *Applied Physics Letters* **98** 163105
- [42] Sauvage S, Boucaud P, Julien F H, Gérard J M and Thierry-Mieg V 1997 *Appl. Phys. Lett.* **71** 2785
- [43] Martí A, Antolín E, Stanley C R, Farmer C D, López N, Díaz P, Cánovas E, Linares P G and Luque A 2006 *Phys. Rev. Lett.* **97** 247701
- [44] Okada Y, Ekins-Daukes N J, Kita T, Tamaki R, Yoshida M, Pusch A, Hess O, Phillips C C, Farrell D J, Yoshida K, Ahsan N, Shoji Y, Sogabe T, and Guillemoles J-F 2015 *Appl. Phys. Rev.* **2**, 021302
- [45] Yoshida M, Ekins-Daukes N J, Farrell D J, and Phillips C C, 2012 *Appl. Phys. Lett.* **100** 263902
- [46] Schaller R D and Klimov V I 2004 *Physical Review Letters* **92** 186601
- [47] Ellingson R J, Beard M C, Johnson J C, Yu P, Micic O I, Nozik A J, Shabaev A and Efros A L 2005 *Nano Lett* **5** 865–871
- [48] Nozik A J 2005 *Inorganic Chem.* **44** 6893
- [49] Shabaev A, Efros A L and Nozik A J 2006 *Nano Letters* **6** 8
- [50] Schaller R D, Pietryga J M and Klimov V I 2007 *Nano Letters* **7** 3469–76
- [51] Murphy J E, Beard M C, Norman A G, Ahrenkiel S P, Johnson J C, Yu P, Micic O I, Ellingson R J and Nozik A J 2006 *Journal of the American Chemical Society* **128** 3241–3247
- [52] Werner J H, Kolodinski S and Queisser H J 1994 *Physical Review Letters* **72** 3851–3854
- [53] Beard M C, Knutsen K P, Yu P, Luther J M, Song Q, Metzger W K, Ellingson R J and Nozik A J 2007 *Nano Letters* **7** 2506–2512
- [54] Hanna M C, and Nozik A 2006 *J. Appl. Phys.* **100** 074510
- [55] Semonin O E, Luther J M, Choi S, Chen H-Y, Gao J, Nozik A J and Beard M C, 2012 *Science* **334**, 1530–1533
- [56] Cunningham P D, Boercker J E, Foos E E, Lumb M P, Smith A R, Tischler J G, and Melinger J S 2011 *Nano Letters* **11** 3476–3481
- [57] Åberg I, Vescovi G, Asoli D, Naseem U, Gilboy J P, Sundvall C, Dahlgren A, Svensson K E, Anttu N, Björk M T and Samuelson L 2016 *IEEE Journal of Photovoltaics* **6** 185–190
- [58] Ziman J M 1960 *Electrons and Phonons* Oxford University Press
- [59] Fröhlich H 1937 *Proc. Roy. Soc. A* **160** 230
- [60] Klemens P 1958, *Solid State Phys* **7** 1
- [61] Lugli P and Goodnick S M 1987 *Phys. Rev. Lett.* **59** 716–719
- [62] Wiener A 2009 *Ultrafast Optics* Wiley
- [63] Tsen K T 2001 *Ultrafast Phenomena in Semiconductors* (K T Tsen, Ed.) Springer Verlag New York Inc. 191–260
- [64] Srinivasan R, Lobastov V A, Ruan C Y, Zewail A H 2003 *Helvetica Chimica Acta.* **86** 1761
- [65] Weathersby S P, Brown G, Centurion M, Chase T F, Coffee R, Corbett J, Eichner J P, Frisch J C, Fry A R, Gühr M, Hartmann N, Hast C, Hettel R, Jobe R K, Jongewaard E N, Lewandowski J R, Li R K, Lindenberg A M, Makasyuk I, May J E, McCormick D, Nguyen M N, Reid A H, Shen X, Sokolowski-Tinten K, Vecchione T, Vetter S L, Wu J, Yang J, Dürr H A and Wang X J 2015 *Review of Scientific Instruments* **86** 073702
- [66] Nozik A J 2001 *Annu. Rev. Phys. Chem.* **52** 193
- [67] Shah J, Pinczuk A, Gossard A C and Wiegmann W 1985 *Phys. Rev. Lett.* **54** 2045–2048
- [68] Rosenwaks Y, Hanna M C, Levi D H, Szymyd D M, Ahrenkiel R K and Nozik A J 1993 *Phys. Rev. B* **48** 14675–14678
- [69] Le Bris A, Lombez L, Laribi S, Boissier G, Christol P and Guillemoles J F 2012 *Energy and Env. Sci.* **5** 6225–6232
- [70] Hirst L C, Fujii H, Sugiyama M, and Ekins-Daukes N J 2014 *IEEE J. Photovoltaics* **4** 244
- [71] Zhang Y, et al. 2016 *Appl. Phys. Lett.* **108**, 131904
- [72] Wang Y, Jackson H E, Smith L M, Burgess T, Paiman S, Gao Q, Tan H H, and Jagadish C 2014 *Nano Lett.* **14** 7153
- [73] Tedeschi D, De Luca M, Fonseca H A, Gao Q, Mura F, Tan H H, Rubini S, Martelli F, Jagadish C, Capizzi M, and Polimeni A 2016 *Nano Lett.* **16** 3085
- [74] Klimov V I 2000 *J. Phys. Chem. B* **104** 6112
- [75] Urayama J, Norris T B, Singh J, Bhattacharya P 2001 *Phys. Rev. Lett.* **85** 4930–4933
- [76] Cooney R R, Sewall S L, Anderson K E H, Dias E A and Kambhampati P 2007 *Phys. Rev. Lett.* **98** 177403
- [77] Seebeck J, Nielsen T R, Gartner P and Jahnke F 2005 *Phys. Rev. B* **71** 125327
- [78] Efros A L and Rosen M 2000 *Annu. Rev. Mater. Sci.* **30** 475
- [79] Lugli P, Bordone P, Reggiani L, Rieger M, Kocever P and Goodnick S M 1989 *Phys. Rev. B.* **39** 7852–7865
- [80] Tsen K S, Wald K R, Ruf T, Yu P Y and Morkoc H 1991 *Phys. Rev. Lett.* **67** 2557–2560
- [81] Tsen K T, Joshi R P, Ferry D K, Botcharev A, Sverdlov B, Salvador A and Morkoc H 1996 *Appl. Phys. Lett.* **68** 2990–2992
- [82] Tsen K T, Kiang J G, Ferry D K, and Morkoc H 2006 *Appl. Phys. Lett.* **89** 112111
- [83] Tsen K T, Kiang J G, Ferry D K, Lu H, Schaff W J, Lin H-W, and Gwo S 2007 *Appl. Phys. Lett.* **90** 152107
- [84] Conibeer G J, Jiang C-W, König D, Shrestha S, Walsh T and Green M A 2008 *Thin Solid Films* **516** 6698
- [85] Conibeer G, Shrestha S, Huang S, Patterson R, Xia H, Feng Y, Zhang P, Gupta N, Tayebjee M, Smyth S, Liao Y, Lin S, Wang P, Dai X and Chung S 2015 *Solar Energy Materials and Solar Cells* **135** 124–129
- [86] Mak K F, Lee C, Hone J, Shan J and Heinz T F 2010 *Phys. Rev. Lett.* **105** 136805
- [87] Xia F, Wang H, Xiao D, Bubey M and Ramasubramaniam A 2014 *Nature Photonics* **8** 899–907
- [88] Price M B, Butkus J, Jellicoe J C, Sadhanala A, Briane A, Halpert J E, Broch K, Hodgkiss J M, Friend R H and Deschler F 2015 *Nat. Commun.* **6** 8420
- [89] Yang Y, Wen X, Xia H, Sheng R, Ma Q, Kim J, Tapping P, Harada T, Kee T W, Huang F, Cheng Y B, Green M, Ho-Baillie A, Huang S, Shrestha S, Patterson R and Conibeer G 2017 *Nat. Commun.* **8** 14120
- [90] Bernardi M 2016 *Eur. Phys. J. B* **89** 2394
- [91] Kadanoff L P and Baym G 1962 *Quantum Statistical Mechanics* W A Benjamin, Inc

- [92] Haug H and Jauho A P 1996 *Quantum Kinetics in Transport and Optics of Semiconductors* Springer
- [93] Mahan 2000 *Many-particle Physics* Springer
- [94] Rossi F and Kuhn T 2002 *Rev. Mod. Phys.* **74** 895
- [95] Haug H and Koch S W 1993 *Quantum Theory of the Optical and Electronic Properties of Semiconductors* World Scientific
- [96] Jacoboni C and Reggiani L 1983 *Rev. Mod. Phys.* **65** 645
- [97] Jacoboni C and Lugli P 1989 *The Monte Carlo Method for Semiconductor Device Simulation* Springer-Verlag
- [98] Hess K 1991 *Monte Carlo Device Simulation: Full Band and Beyond* Kluwer Academic Publ.
- [99] Xu G Lu N Wang W Gao N Ji Z Li L and Liu M 2015 *Organic Electronics* **23** 53
- [100] Lu N Li L and Liu M 2016 *Phys. Chem. Chem. Phys.* **18** 19503
- [101] Fischetti M V and Laux S E 1988 *Phys. Rev. B* **38** 9721
- [102] Saraniti M and Goodnick S M 2000 *IEEE Trans. Elec. Dev.* **47** 1909
- [103] Mazumder S and Majumdar A 2001 *Journal of Heat Transfer* **123** 749-759
- [104] Narumanchi S V J, Murthy J Y and Amon C H 2003 *Journal of Heat Transfer* **136** 946
- [105] Lacroix D, Joulain K and Lemonnier D 2005 *Phys. Rev. B* **72** 064305
- [106] Mittal A and Mazumder S 2010 *Journal of Heat Transfer* **132** 052402
- [107] Mohamed M, Aksamija Z, Vitale W, Hassan F, Park KH and Ravaoli U 2014 *IEEE Trans. Elec.Dev.* **61** 976
- [108] Srivastava GP 1990 *The Physics of Phonons* Taylor & Francis Group
- [109] Sabatti F F M, Goodnick S M and Saraniti M 2017 *J. Heat Transfer* **139** 032002
- [110] See, e.g., Schiff L I 1955 *Quantum Mechanics* McGraw-Hill Inc.
- [111] Ferry D K 1991 *Semiconductors* Macmillan
- [112] Riddoch F A and Ridley B K 1985 *Physica* **134B** 342-346
- [113] Lee I, Goodnick S M, Gulia M, Molinari E and Lugli P 1995 *Phys. Rev. B* **51** 7046-7057
- [114] Takenaka N, Inoue M and Inuishi Y 1979 *J. Phys. Soc. Jap.* **47** 861
- [115] Brunetti R, Jacoboni C, Matulionis A and Dienys V 1985 *Physica* **134B** 369
- [116] Moško M, Mošková A and Cambel V 1995 *Phys. Rev. B* **51** 16860
- [117] Rota L, Rossi F, Goodnick S M, Lugli P, Molinari E and Porod W 1993 *Phys. Rev. B* **47** 1623
- [118] Menoni C S, Buccafusca O, Marconi M C, Patel D, Rocca J J, Robinson G Y, and Goodnick S M, 1997 *Appl. Phys. Lett.* **70** 102-104
- [119] Lee S, Oyafuso F, Allmen P V and Klimeck G 2004 *Phys. Rev. B* **69** 045316
- [120] Hathwar R, Saraniti M and Goodnick S M *Journal of Applied Physics* (to be submitted)
- [121] Lundstrom M 2000 *Fundamentals of Carrier Transport 2nd Edition* Cambridge University Press
- [122] Fischetti M V, Ren Z, Solomon P M, Yang M and Rim K 2003 *Journal of Applied Physics* **94** 1079
- [123] Goodnick S M (2018) Nanotechnology Pathways to Next-Generation Photovoltaics. In: *Semiconductor Nanotechnology, Advances in Information and Energy Processing and Storage*. Nanostructure Science and Technology Series Goodnick S M Korkin A Nemanich R (eds) Springer, New York, NY
- [124] Kamakura Y, Mizuno H, Yamaji M, Morifuji M, Tanaguchi K and Hamaguchi C 1994 *Journal of Applied Physics* **75** 3500
- [125] Fulop W 1967 *Solid-State Electron* **10** 39-43